Geothermics 116 (2024) 102830

Contents lists available at ScienceDirect

Geothermics

journal homepage: www.elsevier.com/locate/geothermics

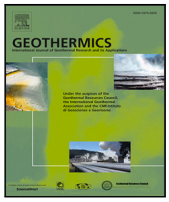

Best practices for characterization of High Temperature-Aquifer Thermal Energy Storage (HT-ATES) potential using well tests in Berlin (Germany) as an example

Guido Blöcher [a,*], Simona Regenspurg [a], Stefan Kranz [a], Martin Lipus [a], Liang Pei [a], Ben Norden [a], Thomas Reinsch [b], Jan Henninges [c], Romy Siemon [d], Dominika Orenczuk [e], Sarah Zeilfelder [f], Traugott Scheytt [g], Ali Saadat [a]

[a] GFZ German Research Centre for Geosciences, Telegrafenberg, 14473 Potsdam, Germany
[b] Fraunhofer-Einrichtung fur Energieinfrastrukturen und Geothermie IEG, Germany
[c] Office for the Safety of Nuclear Waste Management (BASE), Germany
[d] Kummer Erd- und Tiefbau GmbH, 12249 Berlin, Germany
[e] ISAC GmbH, Lützowstraße, 10785 Berlin, Germany
[f] Senatsverwaltung für Umwelt, Mobilität, Verbraucher- und Klimaschutz, 10179 Berlin, Germany
[g] Technical University Bergakademie Freiberg, Gustav-Zeuner-Straße, 09599 Freiberg, Germany

ARTICLE INFO

Keywords:
Aquifer Thermal Energy Storage (ATES)
Push–pull test
Step-rate test
Tracer test
Well test analysis

ABSTRACT

Application of Aquifer Thermal Energy Storage with High Temperatures (HT-ATES) ranging from 60–90 °C is a promising technique to store large amounts of energy in urban areas. However, these areas typically lack information on hydrogeological and thermal parameters of the subsurface to determine the potential for energy storage. Moreover, conventional exploration methods as pumping tests do not account for the variation in density caused by the high temperature gradients or changes in salinity as encountered in HT-ATES operation. The objective of this study is therefore to develop best practices for characterizing the hydrogeological and thermal properties of groundwater wells and their surrounding formation that determine the potential performance of HT-ATES-systems. In addition to conventional pumping tests, a set of Push–Pull tracer Tests (PPTs) with cold and hot water are proposed and scrutinized using Berlin as case study. There, the research well Gt BChb 1/2015, which is characterized by a reservoir temperature of 17 °C at a depth between 220 und 230 m below ground surface was tested.

In 2017, seven Slug-Withdrawal Tests (SWTs), a Step-Rate-Test (SRT), a production tests, and two Push–Pull tracer Tests (PPTs) with hot and cold water were performed during a period of 40 days. These tests were accompanied by Distributed-Temperature-Sensing (DTS) monitoring. The temperature measurements provide indications of injection areas based on the warmback period during a PPT with 81 °C hot water.

The determined aquifer transmissibility $\mathcal{T} = 3.2 \times 10^{-5}$ m^2/s, the related Productivity Index (PI = 2.0 m^3/(h bar)), and maximum flow rates of about 5 m^3/h indicate that the aquifer has potential for HT-ATES. However, the PPT and the DTS monitoring revealed cross flow between the target aquifer and an overlying aquifer. Thus, a new well with a design avoiding cross flow is required to utilize the aquifer's energy storage potential. A set of best practices for characterizing HT-ATES potential was derived from the experiences in this study.

1. Introduction

For storing large amounts of thermal energy over long time periods underground, the concept of seasonal Aquifer Thermal Energy Storage (ATES) seems a promising technology (Bridger and Allen, 2005; Fleuchaus et al., 2018; Dinçer and Rosen, 2010; Lee et al., 1982). Due to their large storage capacity, ATES are particularly suitable for urban areas, where huge amounts of thermal energy are required for heating and cooling of residential areas, office- and industrial buildings.

The feasibility of ATES application is determined on the one hand by the urban infrastructure — especially the availability of a nearby heat source and a district heating pipeline system and on the other hand by the geological aquifer properties. For extracting and injecting large

* Corresponding author.
E-mail address: Guido.Bloecher@gfz-potsdam.de (G. Blöcher).

https://doi.org/10.1016/j.geothermics.2023.102830
Received 23 May 2022; Received in revised form 25 August 2023; Accepted 24 September 2023
Available online 9 October 2023

Nomenclature

Abbreviation

$ATES$	Aquifer Thermal Energy Storage
CFA	Continuous Flow Analysis
CHP	Combined Heat and Power
CoM	Center of Mass
DOC	Dissolved Organic Carbon
DTS	Distributed-Temperature-Sensing
FO	Fiber Optic
$GGUN-FL30$	Flow-through field fluorometer for surface waters
$Gt\ BChb\ 1/2015$	Geothermal borehole Berlin Charlottenburg
HT	High Temperature
$ICP-OES$	Inductively Coupled Plasma-Optical Emission Spectrometry
LT	Low Temperature
NGB	North German Basin
NTU	Nephelometric Turbidity Units
PI	Productivity Index [$m^3/(h\ bar)$]
PPT	Push–Pull Test
PVC	PolyVinyl Chloride
SRT	Step-Rate Test
SWT	Slug-Withdrawal Test
TOC	Total Organic Carbon
TU	Technical University
TVD	True Vertical Depth

Roman symbols

$\dot{Q}$	Heat loss [kW]
$\dot{V}$	Flow rate [m^3/h]
$\mathcal{I}, \mathcal{R}$	Injection and recovery factor
$\mathcal{T}$	Transmissibility [m^2/s]
$\mathcal{X}$	Attenuation factor [–]
a	Dispersivity [m]
B	Linear resistant coefficient [bar h/m^3]
b	Aquifer thickness [m]
C	Non-linear resistant coefficient [bar h^2/m^6]
c	Concentration [mg/L]
c_p	Heat capacity [kJ/(kg K)]
D	Dispersion coefficient [m^2/s]
H	Water level [m]
I	Hydraulic gradient [–]
J, Y	First and second kind Bessel functions [–]
k_f	Hydraulic conductivity [m/s]
l	Length [m]
m	Mass [g]
n	Porosity [–]
p	Pressure [bar]
q	Darcy velocity [m/s]
R	Dimensionless time [–]
r	Radius [m]
S	Coefficient of storage [–]
s	Drawdown [bar]
T	Temperature [°C]
t	Time [s]
U	Fluorescence signals [mV]
u	Variable of integration [–]
v	Velocity [m/s]
$V, \mathcal{V}$	Volume [m^3]

Greek symbols

α	Dimensionless parameter [–]
β	Dimensionless time parameter [–]
λ	Thermal conductivity [W/(m K)]
τ	Time [s]

Other symbols

$'$	Since shut-in
Δ	Difference operator
$\int$	Integral operator
Π	Product operator

Subscript

0	At time zero, initial
$1, 2, 3, \ldots$	Running numbers
a	Groundwater
bg	Background
bh	Borehole
bot	Bottom-hole
c	Casing
d	Duration
e	Effective
H	Horner
i, o	Inner, outer
inj, pro	Injection and production
L	Longitudinal
$L1, L2$	Lamp 1 and 2
max	Maximum
N	Last step
n	Step number
pot	Potential
r	Residual
s	Filter screen
$start, end$	Start and end
wh	Wellhead

Superscripts

$*$	Measured
ad	Admixed
$pull$	Pull phase
$tracer, chaser$	Tracer, chaser
x	Exponent

amounts of heated groundwater into an aquifer, the respective geological formation requires certain properties such as high permeabilities, sufficient thickness and a barrier (aquitard) to aquifers used for drinking water. Therefore, a thorough knowledge on the aquifers thermal, hydraulic, and geochemical properties is important before the heat storage. They are normally determined by hydraulic tests, performed after drilling an ATES well. The challenge in ATES systems as compared to aquifers, used for example for drinking water exploitation, is that the groundwater serves both as a heat carrier and as the heat storage medium, and the specific heat capacity of the ATES is mainly determined by the thermal properties of the fluid and the surrounding rock matrix (Gao et al., 2017). If storage at a higher temperature level is desired, knowledge of the possible temperature driven effects and

interactions with the underground is required to predict the consequences, environmental impact, and optimization of sustainable storage operation.

Well and aquifer tests are usually carried out to obtain information on aquifer properties such as transmissivity, hydraulic conductivity, storativity as well as groundwater velocity and its flow direction. The difference in ATES — as compared to non-ATES groundwater systems is that the ATES well water is typically saline and the injected water will be heated up to 90 °C.

A relatively simple way to determine the near-well aquifer characteristics are slug tests which only require the hydraulic wellhead monitoring over time after quick addition or removal of water (e.g. by pressure drop) from a groundwater well (Zenner, 2009, e.g.). An application for performing these tests for ATES reservoir characterization was not found so far, but it was performed for deep wells in Canada tested for geothermal exploration (Lee et al., 1982, e.g.). Tracer Push–Pull Tests involve the injection of water of known composition and with an added conservative or reactive tracer (e.g. a salt) through a well filter into an aquifer, followed by back-production of this water, during which the tracer composition is analyzed (Istok et al., 1997). For the characterization of an aquifer storage and recovery site, those tests have been performed, both with conservative and reactive tracers (Kruisdijk and van Breukelen, 2021).

Short-duration thermal tracer test have been conducted previously in a shallow sedimentary aquifer with monitoring wells installed in a few meters distance and an injection temperature of 22 °C (Wagner et al., 2013). Similarly, heated water (30 °C) was used as a tracer for understanding transport processes in fractured media by push–pull tracer tests (Klepikova et al., 2016).

Compared to those previous studies, we injected both cold and hot water into an ATES research well of a saline aquifer during push–pull tests, with a maximum injection temperature of 81 °C using both reactive and non-reactive tracers.

This study, therefore aimed to evaluate the effect of ATES-specific groundwater properties (e.g. salinity and temperature variation) on the hydraulic characterization methods for an ATES system by applying a hydraulic testing program. This test program considered Slug-Withdrawal Test (SWT), Step-Rate Test (SRT), and single-well tracer Push–Pull Test (PPT) with different tracers.

The main objectives of the present study are the investigation of the thermal-hydraulic aquifer properties by different test procedures as well as practical issues and remedies to testing difficulties. In particular, a best practice for determining the hydrogeological and thermal parameters of an aquifer for use as an ATES was developed.

2. Materials and methods

Geologically, the area of Berlin is located in the North German Basin (NGB), which is one of the main sedimentary structures in western and central Europe, stretching from England in the west to the eastern border of Poland. The basin formed during Permian times and comprises a huge sedimentary sequence, covering in central parts of the basin more than 7 km of sediments (Hoth and Schretzenmayr, 1993). One characteristic of the basin is the presence of Permian salt structures. The drill site of the well Gt BChb 1/2015 is located at the eastern flank of such a Permian salt structure, which forms a salt pillow, rising upwards from east to west. Due to the lack of detailed geophysical exploration data, the detailed shape of the entire salt structure and the grade of deformation is not known in very detail.

The well was drilled by rotary drilling technique using reverse circulation air injection drilling method until the base of the Rupelian Clay and afterwards a drilling mud was applied consisting of a mixture of Na-Bentonite, Na-carboxymethyl cellulose, calcium carbonate, sodium carbonate and, as a conservative fluorescence tracer, uranine (Regenspurg et al., 2018). In July 2016, after drilling and wellbore completion, first an airlift test and afterwards a production, and a step-rate test were performed that produced altogether about 47 m^3 water and drilling mud-mixture (Regenspurg et al., 2018).

In a final depth of 560 m the well is reaching anhydritic mudstones of the Triassic Grabfeld Formation. Until this depth, the drilling encountered two main aquifer units (Regenspurg et al., 2020). The first aquifer consists of Quaternary to Tertiary formations that are used for domestic water supply and are not permitted for utilization as an aquifer storage. The second aquifer is represented by sandy sediments of the Triassic Exter Formation. The two aquifers are separated from each other by a 85 m-thick clay, the Tertiary (Oligocene) Rupelian Clay. The Rupelian Clay acts as a regional aquitard, disconnecting the shallow drinking water aquifers and the deeper more saline fluids (Fig. 1).

In contrast to the Reichstag aquifer thermal storage (Rockel et al., 1999) located about 2.5 km to the east, no Jurassic sediments are present in the Gt BChb 1/2015 well. Due to the rising salt structure in the deeper surface, the Jurassic aquifers are already thinned out at the current drill site. However, at the base of the Rupelian Clay, approximately one meter of sand was drilled. This sandy unit turns out to be hydraulically active and shows an artesian discharge of about 1 m^3/h. The zone is interpreted as a reworked base horizon of the Oligocene sea (the Rupelbasissand, Regenspurg et al. (2018)). This Rupelbasissand was improperly sealed by cementation and stays hydraulically connected to wellbore via the gravel pack after completion. About 7 m of mudstone separates this sandy unit from the sandstone interval of the Exter Formation, which shows a total thickness b of about 4 m and is located in the depth of 222–226 m below surface. Well logging (gamma density and neutron logs) indicate a mean total porosity of this interval of 0.3 (Regenspurg et al., 2018) and an average effective porosity n_e of around 0.24. The drilling confirmed silty to sandy units also in the deeper part of the well, in the Triassic Stuttgart Formation. These sandy parts represents deposits of a fluvial facies with a more complex geometry. Due to the greater depths and expected worse reservoir properties, these parts were not regarded for the evaluation of an ATES and the well was backfilled with cement to a depth of 260 m. The aforementioned Exter Formation was chosen for the evaluation of an ATES and a filter screen between 220 and 230 m and gravel pack between 214 and 260 m were installed (Fig. 1). The gravel pack of the well extends way further down than the filter screen but does not show a strong influence on the determined hydraulic reservoir characteristics as shown in Appendix C.

Altogether, seven Slug-Withdrawal Tests (SWTs — Section 2.1), a Step-Rate Test (SRT — Section 2.2), and two Push–Pull Tests (PPTs — Sections 2.3 & 2.4) with tracers and hot water were conducted to determine the hydraulic characteristics of the aquifer and their alteration due to simulated thermal storage operations. Therefore, two SWTs were performed before (22.09.17) and five SWTs after (02.11.17) the other hydraulic tests (Table 1). The chosen hydraulic tests are the preferred means to determine well flow capacity in terms of transmissibility, skin effect and storage coefficient. The test assemble used for performing the hydraulic testing is shown in Fig. 2.

The fluid chemistry and microbiological composition of the produced water were analyzed in detail as described by Regenspurg et al. (2020). The water can be classified as NaCl brine with a salinity similar to sea water. Certain trace elements and isotopes measured suggested pyrite oxidation and the contribution of two aquifers to the overall water composition (Regenspurg et al., 2020).

2.1. Slug-Withdrawal Test (SWT)

To generate a sudden pressure drop during the SWTs (Table 1), the wellhead pressure was increased by an air compressor first. To generate 2 bar additional wellhead pressure as done for three SWTs on 02.11.17 it took approximately 15 min. The generation of 5 bar additional wellhead pressure (two SWTs on 22.09.17 and two SWTs on 02.11.17) took approximately 1 h.

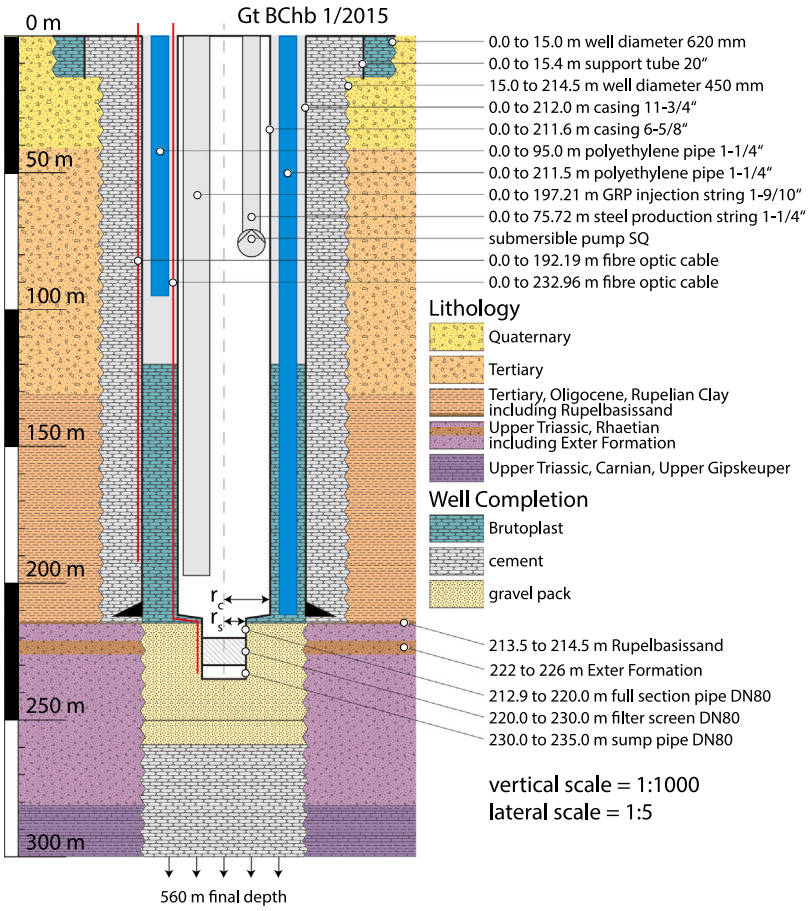

Fig. 1. Design and completion of the well Gt BChb 1/2015 and corresponding lithology.

Table 1
Overview of the seven Slug-Withdrawal Tests (SWTs) carried out and the corresponding wellhead pressure p_{wh} and bottom-hole pressure p_{bot}.

	Time	p_{wh}	p_{bot}	Time	p_{wh}	p_{bot}	Time	p_{wh}	p_{bot}
	SWTs on 22.09.17 with $\Delta p_{wh} = 5$ bar								
	1st			2nd[a]					
Air compression	11:25:50	1.0	8.0	13:59:20	1.0	7.7			
Air release	12:28:45	6.0	8.4	14:46:50	6.1	9.7			
Start build-up	12:29:06	1.0	3.9	14:47:05	1.0	4.6			
End build-up	13:05:48	1.0	7.7	15:16:02	1.0	7.7			
	SWTs on 02.11.17 with $\Delta p_{wh} = 2$ bar								
	3rd			4th			5th		
Air compression	11:38:22	1.1	8.2	12:14:30	1.1	8.2	12:45:40	1.1	8.1
Air release	11:50:12	3.2	8.4	12:31:52	3.1	8.3	13:00:07	3.1	8.1
Start build-up	11:50:16	1.0	6.2	12:31:55	1.0	6.2	13:00:10	1.0	6.1
End build-up	12:10:37	1.1	8.2	12:45:40	1.1	8.1	13:17:22	1.1	8.2
	SWTs on 02.11.17 with $\Delta p_{wh} = 5$ bar								
	6th			7th[a]					
Air compression	13:17:22	1.1	8.2	14:56:46	1.0	8.1			
Air release	14:24:29	6.1	8.3	16:05:07	6.1	8.3			
Start build-up	14:24:36	1.0	3.5	16:05:15	1.0	3.4			
End build-up	14:56:12	1.0	8.1	16:42:16	1.0	8.1			

[a] Not analyzed.

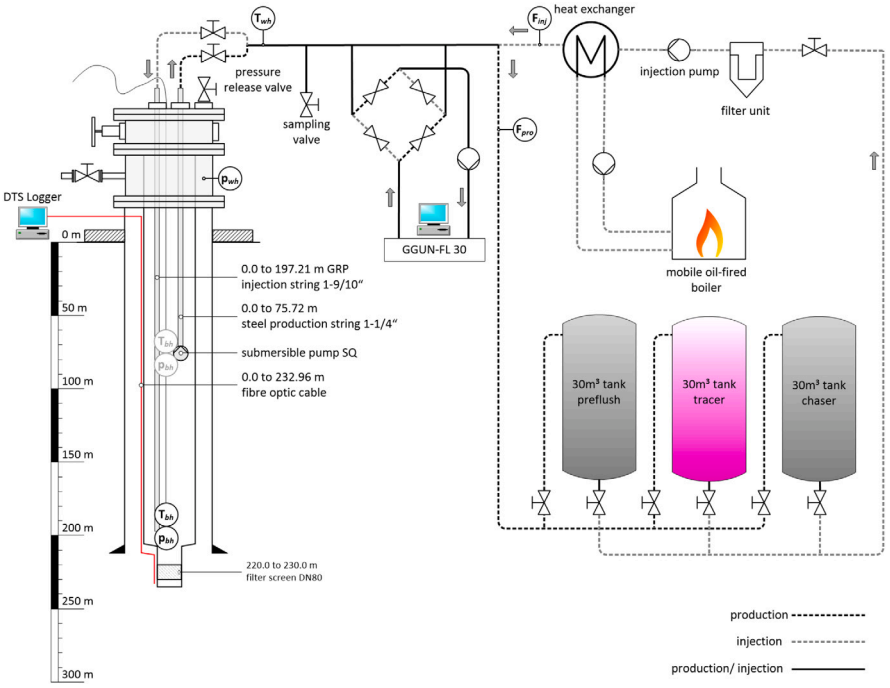

Fig. 2. Flow chart of test assemble.

After achieving the additional wellhead pressure the compressed air was suddenly released by opening a pressure release valve. For the SWTs on 22.09.17 a 1 1/4″ pressure release valve was located 1.35 m above ground. For the second series of SWTs on 02.11.17 a 2″ pressure release valve located 0.8 m below ground level was used. For the SWTs on 22.09.17 the pressure release valve was first opened and then the air compressor was switched off. Due to this procedure, the bottom-hole pressure could not fully equalize and an additional bottom-hole pressure was observed. The 2nd SWT could not be analyzed due to an additional bottom-hole pressure of approximately 2 bar. For the second series of SWTs (02.11.17) the air compressor was first switched off and then waited for the equalization of the bottom-hole pressure. The equalization of the bottom-hole pressure (remaining $\Delta p_{bot} < 0.2$ bar), was observed between 15 and 300 s after switching off the compressor. As soon as the bottom-hole pressure was stabilized the additional wellhead pressure was released. To release 2 bar additional wellhead pressure during the SWTs on 02.11.17 took about 3–4 s. To release 5 bar additional wellhead pressure took 15–21 s and 7–8 s for the SWTs on 22.09.17 and 02.11.17, respectively.

To allow a free movement of the water level the pressure release valve was kept open during the build-up. During the SWTs on 02.11.17 the pressure release valve was located 0.8 m below ground level. When the free moving water level reached this valve, it had to be closed. This closing of the valve slightly influenced the measurements of the bottom-hole pressure at the end of the build-up. The pressure build-up of the 7th SWT indicates some strong influences either by flow resistance close to the borehole or by closing of the valve and was therefore not analyzed. For analyzing the remaining pressure build-up curves in terms of transmissibility and storage coefficient we followed the type curve analyses as outlined in (Cooper et al., 1967):

$$H(t) = \left(\frac{8H_0\alpha}{\pi^2}\right)\int_0^\infty \frac{e^{-\frac{\beta u^2}{\alpha}}du}{u\Delta(u)} \tag{1}$$

$$\Delta(u) = \left[uJ_0(u) + 2\alpha J_1(u)\right]^2 + \left[uY_0(u) + 2\alpha Y_1(u)\right] \tag{2}$$

where H_0 = water level immediately after instantaneous pressure drop; $H(t)$ = water level at time t after instantaneous pressure drop; $\alpha = r_s^2 S/r_c^2$ dimensionless parameter used to determine the coefficient of storage S; $\beta = \mathcal{T}t/r_c^2$ dimensionless time parameter used to determine the transmissibility $\mathcal{T}$. As shown in Fig. 1, r_c = 75.3 mm denotes the radius of casing in the interval over which water level fluctuates and r_s = 40 mm the radius of the filter screen. Fig. 3 shows different curves of H/H_0 as a function of the dimensionless time parameter $\beta = \mathcal{T}t/r_c^2$ in a semi-log plot. Each curve represents a different parameter $\alpha = r_s^2 S/r_c^2$.

To analyze the SWTs, the pressure signal was recorded with a sampling rate of 5 Hz by an electrical pressure transducer, which was suspended in 71 m below ground level. For analyzing the data, a downsampling to 1 Hz was performed. The results of this analysis are shown in Section 3.1.

2.2. Step-Rate Test (SRT)

To determine the productivity index PI and its change due to different flow rates $\dot{V}$ a Step-Rate Test (SRT) with subsequent shut-in was performed on 28.09.17. The measured pressure build-up during the shut-in period 28.09.17 18:52 to 29.09.17 09:49 was analyzed in terms of reservoir transmissibility $\mathcal{T}$. For performing and analyzing the SRT we followed the procedure outlined in Langguth and Voigt (2013). The required submersible pump was installed at the bottom of a 1 1/4″ steel production string in 75.72 m depth (Fig. 2). The bottom-hole pressure p_{bot} was recorded with a sampling rate of 5 Hz by an electrical pressure transducer placed in 210 m depth. A series of five constant-rate productions with rates increasing from 1.95 m³/h to 6.30 m³/h in a step wise fashion was performed (Fig. 4). Each constant-rate step is normally of equal time length, which was approximately 2 h. In total 39.9 m³ were produced.

For each constant-rate step the productivity index PI can be calculated. The productivity index is defined as the flow rate $\dot{V}$ per unit pressure drop s and indicates the production potential of a well. It is defined as:

$$PI = \frac{\dot{V}}{p - p_{bot}} = \frac{\dot{V}}{s}. \tag{3}$$

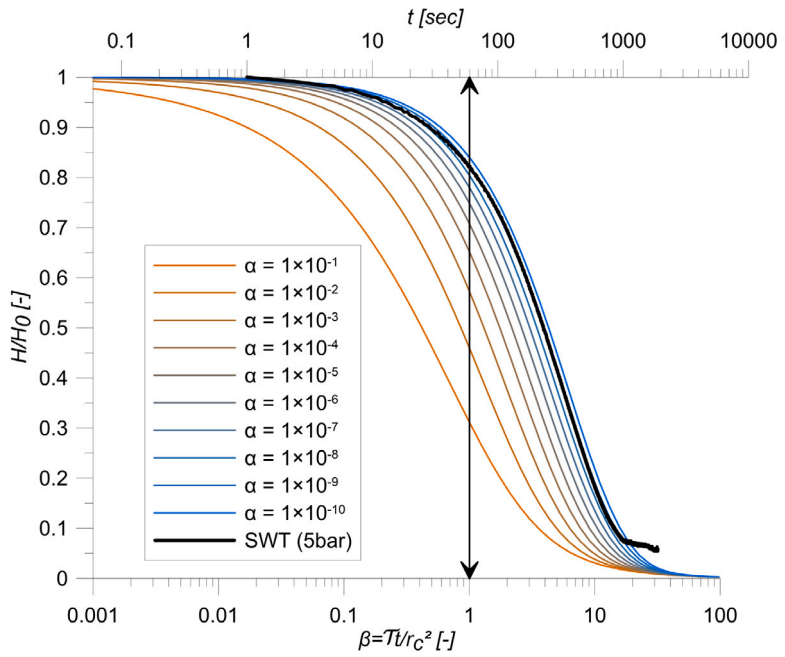

Fig. 3. Type curves for a sudden pressure drop in a well of finite diameter, including an example of a test performed.

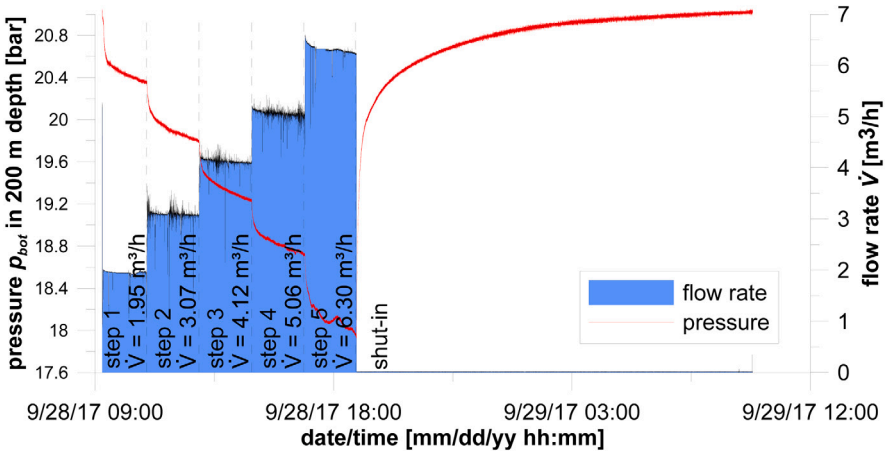

Fig. 4. Performed Step-Rate Test (SRT) with five constant-rate steps and subsequent shut-in including the corresponding bottom-hole pressure p_{bot}.

where p_{bot} is the flowing bottom-hole pressure and $p = 21.05$ bar the average aquifer pressure. In this study, we analyze the PI of the well Gt BChb 1/2015 and its flow rate dependence. The following equation (Jacob, 1947) was used to quantify the linear and non-linear parts of the total drawdown s:

$$s = B\dot{V} + C\dot{V}^2. \tag{4}$$

Based on the calculation of the linear and non-linear resistant coefficient B and C a separation of aquifer and borehole effects on drawdown was performed. The results of this analysis are shown in Section 3.2.

From the build-up data the transmissibility $\mathcal{T}$ was obtained. In general, for build-up tests with a single constant-rate step the Horner semi-log analysis (Horner, 1951) that is the same as the earlier Theis recovery analysis, is used. In a Horner plot the residual drawdown s_r is plotted against the logarithm of the Horner time and from the slope the transmissibility $\mathcal{T}$ can be calculated:

$$s_r = \frac{2.3\dot{V}}{4\pi\mathcal{T}} log\left(\frac{t}{t'}\right), \tag{5}$$

where t is the time since production starts and t' is the time since shut-in.

For a SRT the analysis is similar to Horner semi-log analysis but the residual drawdown s_r is not related to logarithm of the Horner time but to the logarithm of the dimensionless time R, which considers the individual steps (Langguth and Voigt, 2013):

$$R = \prod_{n=1}^{N} \frac{t_n^{\frac{\Delta\dot{V}_n}{\dot{V}_N}}}{t'} = \frac{t_1^{\frac{\Delta\dot{V}_1}{\dot{V}_N}} t_2^{\frac{\Delta\dot{V}_2}{\dot{V}_N}} \dots t_{n-1}^{\frac{\Delta\dot{V}_{n-1}}{\dot{V}_N}} t_n^{\frac{\Delta\dot{V}_n}{\dot{V}_N}}}{t'}, \tag{6}$$

where t_n is the elapsed time since step n starts, $\Delta\dot{V}_n$ is the increment of flow rate at step n, and $\dot{V}_N$ is the flow rate during the last step. For

Table 2
Amount of salts and corresponding tracers used for PPT1 & PPT2.

Salt	Mass [g]	Tracer	Mass m_0^{ad} [g]
		Eosin Y ($C_{20}H_6Br_4Na_2O_5$)	160.0
Sodium nitrate ($NaNO_3$)	3396	Nitrate (NO_3^-)	2477.4
Sodium iodide (NaI)	5992	Iodide (I^-)	5073.0

Table 3
Time schedule, injected and produced volumes as well as the associated flow rates of PPT1.

		Push-phase			Pull-phase[a]
		Pre-flush	Tracer	Chaser	
Start date	[DD.MM.YY]	04.10:17	04.10:17	04.10:17	05.10:17
Start time	[hh:mm]	11:19	16:45	20:51	09:24
End date	[DD.MM.YY]	04.10:17	04.10:17	05.10:17	10.10:17
End time	[hh:mm]	16:45	20:51	00:52	17:08
Duration	[h]	5.4	4.1	4.0	49.0
Volume	[m^3]	28.6	28.0	27.2	315.4
Cumulative volume	[m^3]	28.6	56.6	83.8	315.4
Average flow rate	[m^3/h]	5.3	6.8	6.8	6.4

[a] During the pull-phase of PPT1 the production was paused between 06.10.17 16:53 and 09.10.17 09:14 and between 09.10.17 18:03 and 10.10.17 08:23.

each data point at time t' after shut-in the dimensionless time R was calculated. The residual drawdown s_r was plotted versus the logarithm of the dimensionless time R and the slope of the straight line was used to calculate the transmissibility $\mathcal{T}$:

$$s_r = \frac{2.3\dot{V}_N}{4\pi\mathcal{T}} log(R) \tag{7}$$

For the performed SRT the Horner semi-log analysis as well as the R semi-log analysis were performed and the corresponding results are shown in Section 3.2.

2.3. 1st Push–Pull Test (PPT1)

During the 1st Push–Pull Test (PPT1) 83.8 m^3 were injected (push-phase) and after a hold phase of 8 h and 32 min, 315.4 m^3 were produced (pull-phase). The amount required for the push-phase was previously produced and stored in three closed high tanks with a capacity of 30 m^3 each. The total amount of 83.8 m^3 consists of 23.9 m^3 from a production test (27.09.17 10:21 to 27.09.17 17:32), 39.9 m^3 from the SRT (Section 2.2), and another 20 m^3 from a water pumping between 29.09.17 09:49 and 29.09.17 13:06.

During the filling of the second 30 m^3 high tank, a tracer mixture of eosin Y, iodide, and nitrate (Table 2) was continuously added to the fluid via a feed line. The fluorescent eosin Y and iodide (Meigs and Beauheim, 2001; Schroth et al., 2001) are conservative tracers whereas nitrate is a reactive tracer (Azizian et al., 2005; Istok et al., 1997; Käss, 2004). These tracers were previously mixed with aquifer water in a 250 liter container and stirred with a PVC pipe to guarantee a complete solution of the tracer components. Furthermore, to ensure that the complete 250 liter tracer mixture will enter the high tank, the mixing container was flushed out three times with aquifer water.

The PPT1 started on the 04.10.17 11:19 with the injection (push-phase) into the target horizon. Due to a leaky flange on the wellhead, the injection rate was discontinuous between 11:19 and 13:30. Afterwards, a constant injection rate of 7.2 m^3/h was achieved. During the pre-flush from 11:19 to 16:45, 28.6 m^3 of fluid were injected without a tracer. From 16:45 to 20:51, 28.0 m^3 of the tracer–fluid mixture were injected. Then, from 20:51 to 05.10.17 00:52, another 27.2 m^3 of pure aquifer water was injected as a so-called "chaser". The purpose of the chaser is to push the tracer–fluid mixture out from the well and the gravel pack into the formation. The push-phase lasted 13 h and 33 min and the average injection rate was 6.2 m^3/h.

Table 4
Time schedule, injected and produced volumes with associated flow rates of PPT2.

		Push-phase			Pull-phase
		Pre-flush	Tracer	Chaser	
Start date	[DD.MM.YY]	11.10:17	11.10:17	11.10:17	25.10:17
Start time	[hh:mm]	09:50	14:20	19:30	10:27
End date	[DD.MM.YY]	11.10:17	11.10:17	12.10:17	27.10:17
End time	[hh:mm]	14:20	19:30	00:13	11:37
Duration	[h]	4.5	5.2	4.7	49.2
Volume	[m^3]	29.2	29.0	26.3	305.3
Cumulative volume	[m^3]	29.2	58.2	84.5	305.3
Average flow rate	[m^3/h]	6.5	5.6	5.6	6.2

After a hold phase, the production (pull-phase) started on 05.10.17 09:24. The tracer–fluid mixture was continuously pumped out of the aquifer until 06.10.17 16:53. Due to the still visible eosin Y concentration in the produced water, the pull-phase continued from 09.10.17 09:14 until 10.10.2017 17:08 with an additional break from 09.10.17 18:03 to 10.10.17 08:23. Without the breaks, the pull-phase lasted 49 h and the average production rate was 6.4 m^3/h (Table 3).

During the pull-phase, the fluid was guided through a separator that separates the liquid from the gaseous phase. Subsequently the fluid phase was filtered with a 80 µm filter to ensure a continuous flow through the measuring devices.

2.4. 2nd Push–Pull Test (PPT2) with hot water

PPT2 was conducted in the same manner as PPT1 with the exception that the injected fluid was heated and the temperature change was continuously monitored using a fiber-optic sensor cables installed in the annulus of the borehole (see Section 2.6). Aquifer water from the previous pull-phase of PPT1 was used for the push-phase of PPT2. For this purpose, the last 84.5 m^3 produced water of the previous pull-phase was stored in three closed high tanks. The mixing of the tracer was performed similar to PPT2 but the tracers were stirred with tap water for one hour in a 250 l mixing container and the mixture was then circulated several times in the high tank.

The injection fluid was continuously heated to 70–90 °C using a mobile heater. First, 29.2 m^3 of aquifer water without tracer from the first tank was injected followed by 29.0 m^3 of the tracer–fluid mixture from the second tank. Then 26.3 m^3 of aquifer water from the third tank was replenished as a chaser. The entire injection took place between 11.10.17 09:50 and 12.10.17 00:13 with a flow rate of approximately 5.9 m^3/h. This was followed by the shut-in for 322.2 h until 25.10.17 10:27. Between the 25.10.17 10:27 and 27.10.17 11:37 the pull-phase took place (Table 4). During the pull-phase 305.3 m^3 of aquifer water was continuously pumped for 49.2 h at an average flow rate of 6.2 m^3/h. This produced water was afterwards disposed by discharging into the sewer.

2.5. Tracer sampling, measuring & analysis

2.5.1. Sampling

Altogether, 117 groundwater samples taken during the PPT1 were evaluated. 2 samples were taken directly from the high tank containing the tracer–fluid mixture. Additional 8 samples were taken during the push-phase, 107 samples during the pull-phase via a plastic hose connected to the sampling valve (Fig. 2). Two of the 8 samples at the push-phase were taken during the pre-flush, 4 during the injection of the tracer and another 2 during the injection of the chaser. These 8 samples were filtered and preserved. During the pull-phase, a sample interval of approximately 5 min was selected for the first two hours. In the next five hours, samples were taken every ten minutes. Subsequently, the samples were taken every 30 min until 06.10.17 16:53. At this point, 97 samples have been obtained. Since the flow-through field fluorometer (Section 2.5.3) still showed a clear eosin Y concentration,

the pull-phase was continued on 09.10.17 and 10.10.17 and additional 5 samples were taken for each of the two periods. Therefore, 107 fluid samples from the pull-phase were available for analysis.

For PPT2, 126 groundwater samples were taken and evaluated. Due to the high temperatures and for safety reasons the sampling was performed during the push-phase on the sampling device "FluMo" equipped with a "BIAR sampler" (Milsch et al., 2013). 12 samples were taken for analyzing the push-phase and additional 2 samples were taken directly from the high tank containing the tracer–fluid mixture. 4 of the 12 samples at the push-phase were taken during the pre-flush, 5 during the injection of the tracer and another 3 during the injection of the chaser. These samples were neither filtered nor preserved but stored in chilled brown glass bottles until analysis. Sampling during pull-phase was carried out via an additionally installed hose connection as mentioned before. 112 samples were taken during the pull-phase. Sampling was initially carried out every 10 min. After eight hours, the sampling interval was increased to 30 min for 22 h. For the last 19 h the sampling interval has been increased to 60 min.

2.5.2. Laboratory measurement

All samples were filtered through a 0.45 μm cellulose acetate filter before the measurements. The analysis of the cations was carried out using optical emission spectrometry (ICP-OES/ICAP 6300 Duo from Thermo Fisher Scientific). The anions were measured using the DX 120 ion chromatograph from DIONEX and nitrate (NO_3^-) and ammonium (NH_4^+) with the AutoAnalyzer 3 based on Continuous Flow Analysis (CFA) from Seal Analytical. The Dissolved Organic Carbon (DOC) content was analyzed in the laboratory of water conservation at the TU Berlin with the Vario TOC cube from Elementar. The samples were analyzed by means of ion chromatography according to DIN EN ISO 10 304-1.

To validate the field measurements of eosin Y (Section 2.5.3) without the influence of turbidity, comparative measurements for eosin Y were carried out on the spectral fluorimeter QM-4/2005 (Photon Technology International). Since the samples were stored in chilled brown glass bottles, it can be assumed that there was no significant decrease in fluorescence before the measurement. The spectral fluorimeter has two grating monochromators that allow a continuous change of the excitation and measured emission wavelength and thus a scan of entire spectra. The light source is a 150 watt xenon lamp that is operated in pulsed mode. The analyte is filled into cuvettes and measured. The emission wavelength is measured at a 90° angle. The spectral fluorimeter has a specific working range with a linearity between the fluorescence intensity and the eosin Y concentration. Its lower limit is the detection limit. Above the working range, when the eosin Y concentration is too high, the fluorescence intensity is weakened by self-quenching (Käss, 2004). The working range was determined using a calibration with different eosin Y concentrations of 0, 1, 5, 10, 15, 50 and 100 ppb. Due to fluctuations in the fluorescence maxima for different eosin Y concentrations, the calibration was performed for excitation wavelengths of 531, 532, 533, 534, and 535 nm. A mean value of the corresponding fluorescence intensity was used to generate the calibration curve.

Depending on the expected concentration, the samples were diluted 1:10, 1:100 or 1:300 with an artificial water matrix (25.5 g/L NaCl). Since the sediment load had settled before dilution and measurement, the influence of turbidity was excluded.

2.5.3. Field measurement

For measuring the eosin Y concentration as well as the turbidity of the produced water the GGUN-FL30 flow-through field fluorometer was used (Schnegg, 2002). The GGUN-FL30 flow-through field fluorometer includes four measuring systems, one is dedicated to the measurement of the water turbidity (illumination at 660 nm) while the three others are used to measure the tracer concentrations (with spectral maxima at 370, 470 and 525 nm). Since the aqueous solution of eosin Y exhibits an intense band at 517 nm with a shoulder at 496 nm (Chakraborty and Panda, 2011) the lamp L1 (excitation 470 nm) and lamp L2 (excitation 525 nm) are most suitable for the eosin Y detection. Lamp L3 (excitation 370 nm) was not used in the current study. The calibration of GGUN-FL30 flow-through field fluorometer for a synthetic NaCl solution similar to the produced aquifer fluid is described in detail in Appendix A.

To remove turbidity effects, the GGUN-FL30 was calibrated with different turbid suspensions of 0, 1, 10 and 100 NTU (nephelometric units, formazine standards). The relationship between the optical signal and the turbidity should be linear in log–log space (Schnegg, 2002). Unfortunately, the performed calibration did not provide a clear linear relationship in log–log space. Therefore, the turbidity effect was removed directly based on the field measurements as described in Appendix B.

2.5.4. Analysis

Fluid samples were taken during the push-phases of PPT1 and PPT2 (Section 2.5.1). These samples were analyzed in terms of eosin Y, nitrate, and iodide concentrations. The samples taken during the pre-flush and the injection of the chaser were used to determine the background concentration c_{bg} and the samples taken during the injection of the tracer were used to determine the mean tracer concentration c_0. For PPT1 the background concentration for the artificial tracer eosin Y as well as for nitrate and iodide were below detection limit. Here the measured concentrations c_0^* were considered to be the injected tracer concentrations c_0. Since the produced water (pull-phase) of PPT1 was used for the push-phase of PPT2 and the same tracers were admixed, the background concentrations of these tracers must be considered for the push-phase of PPT2. Here the injected tracer concentration was calculated as the difference between the measured tracer concentration and the corresponding background concentration $c_0 = c_0^* - c_{bg}$. Based on the determined tracer concentrations, the injected tracer mass m_0 was derived:

$$m_0 = \int_{t_{start}^{tracer}}^{t_{end}^{tracer}} c_0(t)\dot{V}(t)dt, \tag{8}$$

with t_{start}^{tracer} and t_{end}^{tracer} as the starting and ending time of tracer injection and $\dot{V}$ as the injection flow rate. Since the tracer concentrations during injection were considered as constant value (mean tracer concentrations) the injected tracer masses can be approximated:

$$m_0 = c_0 V_{inj}^{tracer}, \tag{9}$$

with V_{inj}^{tracer} as the total injected volume of the tracer–fluid mixture. Furthermore, the injection factor $\mathcal{I}$ of the tracers can now be defined as the ratio between the injected tracer mass m_0 and the admixed tracer mass m_0^{ad}:

$$\mathcal{I} = \frac{m_0}{m_0^{ad}}. \tag{10}$$

The measured tracer and background concentrations as well as injected tracer masses are summarized in Table 5.

During the pull-phase of PPT1 and PPT2, 107 and 112 samples respectively were collected and analyzed for eosin Y, nitrate, and iodide. Furthermore the concentration of eosin Y was monitored with GGUN-FL30 flow-through field fluorometer (see Section 2.5.3). Using the measured tracer concentrations c and the corresponding production rate $\dot{V}$, the recovered tracer mass m can derived:

$$m = \int_{t_{start}^{pull}}^{t_{end}^{pull}} c(t)\dot{V}(t)dt, \tag{11}$$

with t_{start}^{pull} and t_{end}^{pull} as the starting and ending time of the pull-phase. The recovery factor $\mathcal{R}$ of the tracers can now be defined as the ratio between the recovered tracer mass m and the injected tracer mass m_0:

$$\mathcal{R} = \frac{m}{m_0}. \tag{12}$$

Table 5
Mean tracer concentration during injection phase of PPT1 and PPT2.

		Eosin Y	Nitrate	Iodide
1st Push–Pull Test (PPT1)				
Analyzed samples (tracer)		4	4	3
Mean tracer concentrations c_0	[mg/L]	4.668 (±0.187)	78.398 (±1.018)	90.500 (±27.752)
Injected tracer mass m_0	[g]	130.7	2194.7	2533.5
2nd Push–Pull Test (PPT2)				
Analyzed samples (tracer)		5	5	2
Measured tracer concentrations c_0^*	[mg/L]	5.589 (±0.071)	94.422 (±0.028)	94.900 (±28.100)
Analyzed samples (pre-flush & chaser)		7	7	2
Measured background concentrations c_{bg}	[mg/L]	0.081 (±0.007)	0.536 (±0.204)	1.300 (±0.100)
Mean tracer concentrations $c_0 = c_0^* - c_{bg}$	[mg/L]	5.508	93.886	93.600
Injected tracer mass m_0	[g]	159.8	2724.3	2716.0

Based on the measured tracer concentrations and their time dependency, parameters such as average groundwater velocity v_a, longitudinal dispersivity a_L, longitudinal dispersion coefficient $D_L = v_a a_L$, hydraulic gradient I, and attenuation factor $\mathcal{X}$ can be derived. For a single-well PPT the displacement of the tracer due to injection, drift, and production must be taken into account.

2.5.4.1. Radius of tracer front r. If we consider a confined aquifer, which is homogeneous and isotropic, and the natural groundwater flow is negligible, the cylindrical volume of water injected into the aquifer is given by:

$$V = \pi r^2 b n_e, \tag{13}$$

with r as the radius of the cylinder, b as the thickness of the aquifer, and n_e as the effective porosity. Based on this equation the radius r of the tracer front was determined.

The injected volume V into the aquifer is the difference between the injected volume into the well V_{inj} and the volume which remains in the borehole V_{bh}. At the end of the push-phase, the volume injected into the well is the volume of the tracer–fluid mixture plus the volume of the chaser $V_{inj} = V_{inj}^{tracer} + V_{inj}^{chaser}$. Since an injection string was used for the push-phase (Fig. 1), the volume of the borehole was reduced to $V_{bh} = 0.74$ m^3. The maximum radius of the tracer front at the end of the push-phase is given by:

$$r_{max} = \sqrt{\frac{V_{inj} - V_{bh}}{\pi b n_e}}. \tag{14}$$

The injected volume V_{inj} during PPT1 and PPT2 is 55.2 m^3 and 55.3 m^3, respectively. Considering an aquifer thickness of $b = 4$ m and an effective porosity $n_e = 0.24$ (Section 1) the maximum radius of the tracer front is $r_{max} = 4.28$ m for both tests.

2.5.4.2. Average groundwater velocity v_a, Darcy velocity q, and hydraulic gradient I. Various methods are known allowing to determine the average groundwater velocity v_a from the tracer data (e.g. Leibundgut et al., 2009; Leibundgut and Seibert, 2011; Leap and Kaplan, 1988; Paradis et al., 2017). For a single-well PPT the methods developed by Leap and Kaplan (1988) and Paradis et al. (2017) seem most applicable. Based on the method of Leap and Kaplan (1988) the average groundwater velocity can be calculated as follows:

$$v_a = \frac{\sqrt{\frac{\mathcal{V}_{pro}}{\pi b n_e}}}{(t_d + \tau_{pro})}, \tag{15}$$

with $\mathcal{V}_{pro}$ as the volume at which one-half of the mass of the tracer has been recovered, t_d as the time elapsed from the end of push-phase until the start of pull-phase, and τ_{pro} as the corresponding time of the pull-phase at which $\mathcal{V}_{pro}$ occurs. Eq. (15) does not account for the transport of tracer during the injection phase. Therefore, Paradis et al. (2017) developed Eq. (16), very similar to the one of Leap and Kaplan (1988), which account for the transport of tracer during the injection phase:

$$v_a = \frac{\sqrt{\frac{\mathcal{V}_{pro} - \mathcal{V}_{inj}}{\pi b n_e}}}{(\tau_{inj} + t_d + \tau_{pro})}, \tag{16}$$

with $\mathcal{V}_{inj}$ as the volume of water injected until the center of mass of the tracer is released, and τ_{inj} as the corresponding time of the push-phase at which $\mathcal{V}_{inj}$ occurs. To prove if the transport of the tracer during the injection phase is negligible both methods were used to derive the average groundwater velocity v_a. If the transport of the tracer during the injection phase is not negligible, then Eq. (16) will yield lower values than Eq. (15).

The average groundwater velocity v_a is related to the Darcy velocity q by the effective porosity n_e and takes the form:

$$v_a = \frac{q}{n_e}. \tag{17}$$

Assuming unidirectional groundwater flow and laminar flow conditions, the hydraulic gradient I can be obtained based on the hydraulic conductivity k_f by applying Darcy's law:

$$q = k_f I. \tag{18}$$

2.5.4.3. Attenuation factor $\mathcal{X}$, Longitudinal dispersivity a_L, and dispersion coefficient D_L. To determine the longitudinal dispersivity a_L we followed the procedure outlined in Gelhar and Collins (1971), which is a type curve method:

$$\frac{c}{c_0} = \frac{1}{2} erfc \left\{ \frac{\left(\frac{V_{pro}}{V_{inj}} - 1\right)}{\sqrt{\frac{16}{3}\frac{a_L}{r_{max}}\left(2 - \sqrt{1 - \frac{V_{pro}}{V_{inj}}}\left(1 - \frac{V_{pro}}{V_{inj}}\right)\right)}} \right\}, \tag{19}$$

with c_0 as the mean tracer concentration during the injection of the tracer and c as the tracer concentration during the pull-phase. $V_{inj} = V_{inj}^{tracer} + V_{inj}^{chaser}$ as the injected volume after the tracer has been mixed in and thus corresponds to the injected volume without the pre-flush phase. V_{pro} as the cumulative volume produced and r_{max} as the maximum radius of the tracer front as mentioned above. From Eq. (19) it can be seen that the ratio $\frac{c}{c_0}$ is 0.5 if the volume produced corresponds to the injected volume $V_{pro} = V_{inj}$. The ratio $\frac{c}{c_0}$ at this point is independent of the dispersivity a_L:

$$\left(\frac{c}{c_0}\right)_{\frac{V_{pro}}{V_{inj}}=1} = \frac{1}{2}. \tag{20}$$

If the ratio is less than 0.5 an additional attenuation by aquifer cross-flow must be considered. The corresponding attenuation factor $\mathcal{X}$ is given by:

$$\mathcal{X}\left(\frac{c}{c_0}\right)_{\frac{V_{pro}}{V_{inj}}=1} = \frac{1}{2} \Rightarrow \mathcal{X} = \frac{1}{2}\left(\frac{c_0}{c}\right)_{\frac{V_{pro}}{V_{inj}}=1}. \tag{21}$$

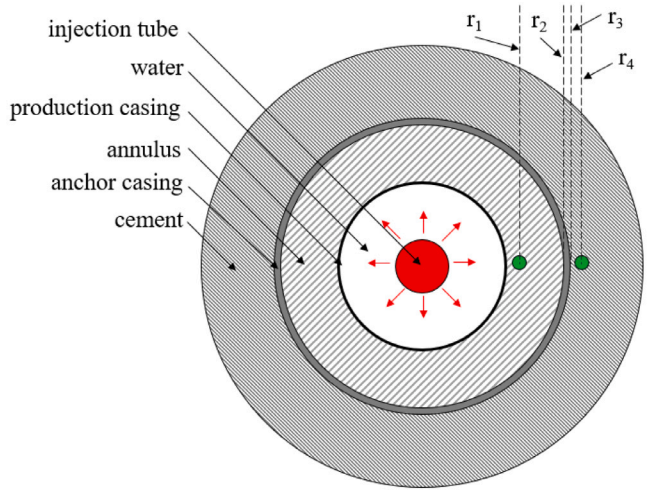

Fig. 5. Downhole fiber-optic cable configuration.

We used the attenuation factor $\mathcal{X}$ to modify Eq. (19), making it possible in this study to calculate the dispersivity a_L even for attenuated tracer–fluid mixtures:

$$\mathcal{X}\frac{c}{c_0} = \frac{1}{2} erfc \left\{ \frac{\left(\frac{V_{pro}}{V_{inj}} - 1\right)}{\sqrt{\frac{16}{3}\frac{a_L}{r_{max}}\left(2 - \sqrt{1 - \frac{V_{pro}}{V_{inj}}}\left(1 - \frac{V_{pro}}{V_{inj}}\right)\right)}} \right\}. \quad (22)$$

In Eq. (22), the dispersivity a_L was changed until there was a best correlation between the associated type curve and the measured concentration ratio $\frac{c}{c_0}$. Since the tracer concentration at the beginning of the pull-phase was strongly influenced by the injected chaser, this correlation was performed for the tailing of the tracer concentration curve with $V_{pro} > V_{inj}$. The obtained dispersivity was used to calculate the longitudinal dispersion coefficient D_L:

$$D_L = v_a a_L. \quad (23)$$

2.6. Distributed Temperature Sensing (DTS)

Fiber-optic Distributed Temperature Sensing, or DTS, describes the technology of using each location of a glass fiber as a sensor for temperature measurement. This is done by coupling optical pulses into a glass fiber and measuring the backscattered light as a function of time. Given the two-way travel time and the speed of light in the glass fiber, a physical origin of the Raman backscattering location can be determined.

2.6.1. Fiber-optic cable configuration

Two fiber-optic cables were permanently installed in the well (Fig. 1). The outer cable was installed in the annulus behind the 11 3/4″ steel anchor casing to a depth of 192 m. The cable was installed in a loop so that both cable ends are accessible at surface. Centralizers were installed at every third joint to protect the cable during installation. The cable was mounted twice per casing joint (every 6 m) using a pneumatic strapping tool and a 3 mm spacer between cable and casing. The inner fiber-optic cable was installed single-ended along the (6 5/8″ × 4 1/2″) production casing to a depth of 233 m. Fig. 5 shows a schematic cross section of the well in the 6 5/8″ interval. DTS data were constantly measured before, during and after the hot water injection test (and fluid production test) with a spatial resolution of 0.5 m and a temporal resolution of 40 seconds.

Table 6
Thermal conductivity and spatial arrangement of different layers in the well with radii according to Fig. 5.

Thermal conductivity	Material	W/(m K)
$\lambda_{1.0}$	Air	0.02
$\lambda_{1.1}$	Water	0.6
$\lambda_{1.2}$	Brutoplast	1.624
λ_2	Steel (C95 Hydril)	46
λ_3	Cement (Portland Class G)	1.5
Radius	**Location**	**m**
r_1	FO cable on prod. casing	0.086
r_2	Anchor casing (inner diameter)	0.135
r_3	Anchor casing (outer diameter)	0.149
r_4	Cement (3 mm)	0.152

2.6.2. Well heat transition calculation

Given the configuration of the two fiber-optic cables in the well, a measurement of the radial temperature gradient is possible along the well during hot water fluid injection testing and during fluid production testing. When quasi-steady temperature conditions between both annuli are reached, the temperature gradient can be used to calculate the heat loss over the well. According to the Gnielinski (2013), the radial heat loss along a cylinder of different layers under steady conditions can be calculated with

$$\dot{Q} = \frac{2\pi l(T_i - T_o)}{\frac{1}{\lambda_1} ln\frac{r_2}{r_1} + \frac{1}{\lambda_2} ln\frac{r_3}{r_2} + \cdots + \frac{1}{\lambda_n} ln\frac{r_{n+1}}{r_n}}, \quad (24)$$

with $\dot{Q}$ as the heat loss, l as the length, T_i and T_o as the inner and outer temperature, λ as the material specific thermal conductivity, and r as the radial distances according to Fig. 5. The values for the parameters λ and r can be found in Table 6.

As the radial distance between both DTS cables is small, we estimate a quasi-static temperature difference between both cables during later stages of the hot fluid injection and production and can show this for the field data in Appendix D.

3. Results

3.1. Slug-Withdrawal Test (SWT)

Five out of seven SWTs were analyzed. As shown in Table 7 the determined transmissibility varies in a range between 5.67×10^{-5} and 9.45×10^{-5} m^2/s. By comparing the 1st SWT on 22.09.17 with the 7th on 02.11.17 no measurable difference either in transmissibility nor in the storage coefficient could be observed. Both tests were performed with a sudden pressure drop of approximately 5 bar. In contrast, the storage coefficient S for the individual tests varies by six orders of magnitude. The obtained values for SWTs with 2 bar pressure drop are 1.000.000 times higher than the values obtained during SWTs with 5 bar pressure drop. However, as mentioned by Cooper et al. (1967) the analysis of the storage coefficient by SWTs has questionable reliability. Furthermore, due to the different pressure drops applied, the corresponding coverage radius will be different. In the vicinity of the well a high heterogeneity in terms of storage coefficient in radial direction exist (borehole, gravel pack, aquifer) which influences the measurement.

3.2. Step-Rate Test (SRT)

For each of the five steps of the SRT the average flow rate $\dot{V}$ was calculated and the corresponding pressure drawdown s at the end of the step was determined. Based on Eq. (3) the productivity index PI for each single step was derived (Table 8).

The productivity index shows a flow rate dependency and decreases from 2.83 m^3/(h bar) to 2.03 m^3/(h bar) as flow rate increases from 1.95 m^3/h to 6.30 m^3/h. Therefore, flow rate and drawdown data were

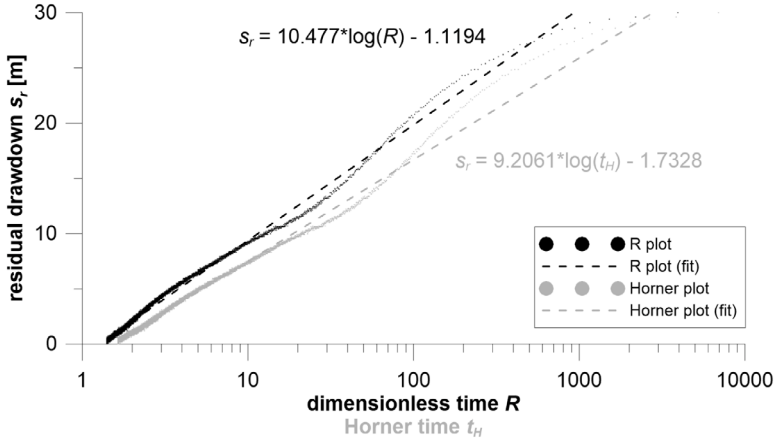

Fig. 6. Semi-log analysis of the residual drawdown during the shut-in of the Step-Rate Test (SRT).

Table 7
Transmissibility $\mathcal{T}$ and storage coefficient S as well as time $t_{\beta=1}$ and dimensionless parameter α determined for the SWTs on 22.09.17 and 02.11.17. The radius of casing and the filter screen are $r_c = 75.3$ mm and $r_s = 40$ mm, respectively.

SWT	Date [DD.MM.YY]	Δp_{wh} [bar]	$t_{\beta=1}$ [s]	$\mathcal{T} = \frac{r_c^2}{t_{\beta=1}}$ [m²/s]	α [–]	$S = \frac{r_c^2}{r_s^2}\alpha$ [–]
1st	22.09.17	5	60	9.45×10^{-5}	1×10^{-9}	3.54×10^{-9}
2nd	22.09.17	5	Not analyzed			
3rd	02.11.17	2	89	6.37×10^{-5}	1×10^{-3}	3.54×10^{-3}
4th	02.11.17	2	90	6.30×10^{-5}	1×10^{-3}	3.54×10^{-3}
5th	02.11.17	2	100	5.67×10^{-5}	1×10^{-3}	3.54×10^{-3}
6th	02.11.17	5	Not analyzed			
7th	02.11.17	5	60	9.45×10^{-5}	1×10^{-9}	3.54×10^{-9}

Table 8
Average flow rate $\dot{V}$, corresponding pressure drawdown s (determined at a depth of 210 m) and calculated productivity index PI for each step of the SRT on 28.09.17. In addition, the linear $B\dot{V}$ and non-linear $C\dot{V}^2$ drawdown quantities are shown.

Step	$\dot{V}$ [m³/h]	s [bar]	PI [m³/(h bar)]	$B\dot{V}$ [bar]	$C\dot{V}^2$ [bar]	$B\dot{V} + C\dot{V}^2$ [bar]
1	1.95	0.69	2.83	0.62	0.11	0.73
2	3.07	1.25	2.46	0.98	0.26	1.24
3	4.12	1.82	2.26	1.32	0.47	1.79
4	5.06	2.33	2.17	1.62	0.71	2.33
5	6.30	3.11	2.03	2.01	1.11	3.12

used to separate linear and non-linear pressure losses. A parametrization of Eq. (4) by curve fitting (coefficient of determination R-squared = 0.9993) led to a linear resistant coefficient $B = 3.194 \times 10^{-1}$ bar h/m³ and a non-linear resistant coefficient $C = 2.792 \times 10^{-2}$ bar h²/m⁶. Based on these resistant coefficients, the linear $B\dot{V}$ and non-linear $C\dot{V}^2$ drawdown quantities were determined (Table 8). At high flow rates the non-linear pressure losses were more pronounced. For step five the non-linear pressure losses led to an additional drawdown of 1.11 bar, which is more than one-third of the total drawdown. Furthermore, the linear part of the drawdown was used to calculate the potential of the aquifer productivity $PI_{pot} = 1/B = 3.13$ m³/(h bar). This potential could be achieved for a perfect well without any non-linear pressure losses.

During shut-in the build-up data were recorded and analyzed by both, Horner semi-log analysis as well as dimensionless time R analysis (Fig. 6).

Although the dimensionless time R considers the characteristics of the individual steps, both analyses provide similar results. For one logarithmic cycle of the dimensionless time $log(R) = 1$ the water table rises by 10.5 m. In contrast, for one logarithmic cycle of the Horner time $log(t_H) = 1$ the water table rises by 9.2 m. Substituting these values in Eqs. (7) and (5) results in a transmissibility of $\mathcal{T} = 3.06 \times 10^{-5}$ m²/s (R semi-log analysis) and $\mathcal{T} = 3.48 \times 10^{-5}$ m²/s (Horner semi-log analysis), respectively.

3.3. Push-Pull Tests (PPTs)

The results of both PPTs are summarized in Tables 9 and 10. The injection factor $\mathcal{I}$ for PPT1 varies between 49.9% for iodide and 88.6% for nitrate For eosin Y the injection factor is about 81.7%. For PPT2 the injection factor for iodide is 53.5%, for eosin Y 99.9%, and for nitrate 110%. Although the tracer concentrations were corrected using the determined background concentrations, the rinsing of the high tank during PPT2 significantly increases the amount of the injected tracers. For eosin Y and nitrate the total admixed tracer masses were injected during PPT2.

The recovery factor $\mathcal{R}$ indicates the fraction of the tracer which could be recovered during the pull-phase in comparison with the injected tracer masses. For the PPT1 the recovery factor varies between 56.1% and 65.3%. For PPT2 the recovery factor is further reduced and only 50.4% to 55.1% could be recovered. This reduced recovery factor could potentially linked to the shut-in time t_d between the end of push-phase until the start of pull-phase. This shut-in time was 512 min for PPT1 and 19 335 min for PPT2.

To derive quantities for the groundwater velocity v_a the Center of Mass (CoM) at which one-half of the tracer mass has been released or recovered must be determined (Figs. 7 and 9). For both PPTs a constant injection concentration for all tracers was assumed. Therefore, the CoM is released after one-half of the tracer–fluid mixture was injected. The corresponding volume $\mathcal{V}_{inj}$ was 13.9 m³ and 14.4 m³ for PPT1 and PPT2, respectively. The elapsed time τ_{inj} between the start of the tracer injection and the time at which one-half of the tracer has been released was 123 min and 155 min for PPT1 and PPT2, respectively. The volume $\mathcal{V}_{pro}$ at which one-half of the tracer mass has been recovered was 48.6 m³ (iodide), 53.7 m³ (nitrate), and 66.1–74.2 m³ (eosin Y) for PPT1. The corresponding time τ_{pro} between the start of the pull-phase and the time at which one-half of the tracer has been recovered was 435 min (iodide), 481 min (nitrate), and 598-671 min (eosin Y). For PPT2 the volume $\mathcal{V}_{pro}$ at which one-half of the tracer mass has been recovered was 52.2 m³ (nitrate), 53.1 m³ (iodide), and 76.2–83.1 m³ (eosin Y). The required time τ_{pro} to recover one-half of the tracers for PPT2 was a bit longer in comparison to PPT1 and took 482 min (nitrate), 491 min (iodide), and 710-776 min (eosin Y). Based on the Eqs. (15) and (16) the average groundwater velocity v_a was calculated on the one hand, neglecting the drift during injection (Leap and Kaplan, 1988) and on the other hand, taking the drift during injection into account (Paradis et al., 2017). Considering the tracer drift during injection led to lower values of average groundwater velocity that indicates that the transport of the tracer during the injection

Table 9
Results of the PPT1. For the calculations, a transmissibility of $\mathcal{T} = 4.0 \times 10^{-5}$ m^2/s, an aquifer thickness of $b = 4$ m, a hydraulic conductivity $k_f = \mathcal{T}/b = 1.0 \times 10^{-5}$ m/s and an effective porosity of $n_e = 0.24$ were used.

		Eosin Y (laboratory)	Eosin Y (fluorometer)	Nitrate (laboratory)	Iodide (laboratory)
Injection $\mathcal{I}$ & recovery factor $\mathcal{R}$					
Admixed tracer mass m_0^{ad}	[g]	160.0	160.0	2477.4	5073.0
Injected tracer mass m_0	[g]	130.7	130.7	2194.7	2533.5
Recovered tracer mass m	[g]	73.3	79.3	1432.5	1424.9
Injection factor $\mathcal{I} = m_0/m_0^{ad}$	[%]	81.67	81.67	88.59	49.94
Recovery factor $\mathcal{R} = m/m_0$	[%]	56.10	60.67	65.27	56.24
Groundwater velocity v_a					
Volume $\mathcal{V}_{inj}$ [a]	[m^3]		13.89		
Volume $\mathcal{V}_{pro}$ [b]	[m^3]	66.13	74.15	53.65	48.62
Time τ_{inj} [c]	[min]		123		
Time τ_{pro} [d]	[min]	598	671	481	435
Time t_d [e]	[min]		512		
Velocity v_a (Leap and Kaplan, 1988)	[m/s]	7.03×10^{-5}	6.99×10^{-5}	7.08×10^{-5}	7.07×10^{-5}
Velocity v_a (Paradis et al., 2017)	[m/s]	5.63×10^{-5}	5.70×10^{-5}	5.42×10^{-5}	5.29×10^{-5}
Darcy velocity q & hydraulic gradient I based on groundwater velocity according to Paradis et al. (2017)					
Darcy velocity q	[m/s]	1.35×10^{-5}	1.37×10^{-5}	1.30×10^{-5}	1.27×10^{-5}
Hydraulic gradient I	[m/m]	1.35	1.37	1.30	1.27
Attenuation factor $\mathcal{X}$, longitudinal dispersivity a_L, & longitudinal dispersion coefficient D_L					
Attenuation factor $\mathcal{X}$	[–]	3.8	3.9	2.6	3.4
Longitudinal dispersivity a_L	[m]	0.82	1.05	0.63	0.24
Longitudinal dispersion coefficient D_L	[m^2/s]	4.61×10^{-5}	5.99×10^{-5}	3.42×10^{-5}	1.27×10^{-5}

[a] Volume $\mathcal{V}_{inj}$ at which one-half of the tracer mass has been released.
[b] Volume $\mathcal{V}_{pro}$ at which one-half of the tracer mass has been recovered.
[c] Elapsed time τ_{inj} between the start of the tracer injection and $\mathcal{V}_{inj}$.
[d] Elapsed time τ_{pro} between the start of the pull-phase and $\mathcal{V}_{pro}$.
[e] Elapsed time t_d between the end of push-phase until the start of pull-phase.

Table 10
Results of the PPT2. For the calculations, a transmissibility of $\mathcal{T} = 4.0 \times 10^{-5}$ m^2/s, an aquifer thickness of $b = 4$ m, a hydraulic conductivity $k_f = \mathcal{T}/b = 1.0 \times 10^{-5}$ m/s and an effective porosity of $n_e = 0.24$ were used.

		Eosin Y (laboratory)	Eosin Y (fluorometer)	Nitrate (laboratory)	Iodide (laboratory)
Injection $\mathcal{I}$ & recovery factor $\mathcal{R}$					
Admixed tracer mass m_0^{ad}	[g]	160.0	160.0	2477.4	5073.0
Injected tracer mass m_0	[g]	159.8	159.8	2724.3	2716.0
Recovered tracer mass m	[g]	80.6	88.0	1411.1	1385.8
Injection factor $\mathcal{I} = m_0/m_0^{ad}$	[%]	99.90	99.90	109.96	53.54
Recovery factor $\mathcal{R} = m/m_0$	[%]	50.41	55.08	51.80	51.02
Groundwater velocity v_a					
Volume $\mathcal{V}_{inj}$ [a]	[m^3]		14.43		
Volume $\mathcal{V}_{pro}$ [b]	[m^3]	76.18	83.10	52.19	53.13
Time τ_{inj} [c]	[min]		155		
Time τ_{pro} [d]	[min]	710	776	482	491
Time t_d [e]	[min]		19 335		
Velocity v_a (Leap and Kaplan, 1988)	[m/s]	4.18×10^{-6}	4.35×10^{-6}	3.50×10^{-6}	3.53×10^{-6}
Velocity v_a (Paradis et al., 2017)	[m/s]	3.73×10^{-6}	3.92×10^{-6}	2.95×10^{-6}	2.99×10^{-6}
Darcy velocity q & hydraulic gradient I based on groundwater velocity according to Paradis et al. (2017)					
Darcy velocity q	[m/s]	8.96×10^{-7}	9.42×10^{-7}	7.09×10^{-7}	7.17×10^{-7}
Hydraulic gradient I	[m/m]	0.09	0.09	0.07	0.07
Attenuation factor $\mathcal{X}$, longitudinal dispersivity a_L, & longitudinal dispersion coefficient D_L					
Attenuation factor $\mathcal{X}$	[–]	4.6	4.4	2.9	5.6
Longitudinal dispersivity a_L	[m]	1.17	1.39	0.33	0.49
Longitudinal dispersion coefficient D_L	[m^2/s]	4.37×10^{-6}	5.45×10^{-6}	9.74×10^{-7}	1.46×10^{-6}

[a] Volume $\mathcal{V}_{inj}$ at which one-half of the tracer mass has been released.
[b] Volume $\mathcal{V}_{pro}$ at which one-half of the tracer mass has been recovered.
[c] Elapsed time τ_{inj} between the start of the tracer injection and $\mathcal{V}_{inj}$.
[d] Elapsed time τ_{pro} between the start of the pull-phase and $\mathcal{V}_{pro}$.
[e] Elapsed time t_d between the end of push-phase until the start of pull-phase.

phase is not negligible. For PPT1 the average groundwater velocity of $v_a = 5.29 - 5.70 \times 10^{-5}$ m^3/s considering the drift during injection and $v_a = 6.99 - 7.08 \times 10^{-5}$ m^3/s neglecting this drift was obtained. For PPT2 the calculated groundwater velocities were much lower. An average groundwater velocity of $v_a = 2.99 - 3.92 \times 10^{-6}$ m^3/s considering the drift during injection and $v_a = 3.50 - 4.35 \times 10^{-6}$ m^3/s neglecting this drift was obtained. For both PPTs these obtained values are consistent and independent of the used tracers.

Based on the groundwater velocities that consider the drift during injection, the Darcy velocity q as well as the hydraulic gradient I were

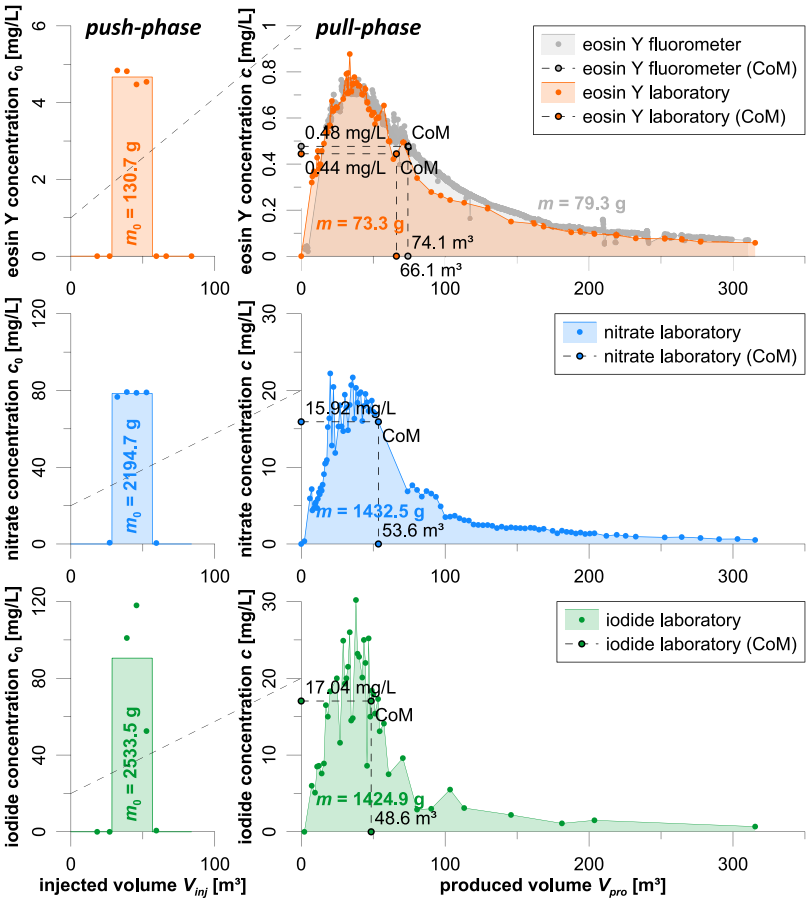

Fig. 7. Determined eosin Y, nitrate, and iodide concentrations during the 1st Push–Pull Test (PPT1). For each tracer the Center of Mass (CoM) at which one-half of the mass of the tracer has been recovered is indicated.

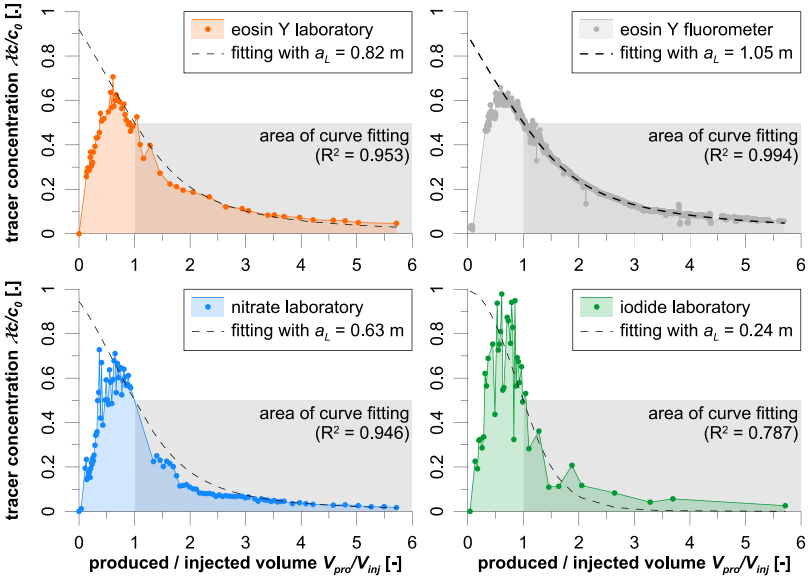

Fig. 8. Type curve analysis to determine the longitudinal dispersivity a_L for the 1st Push–Pull Test (PPT1). The curve fitting was performed for the tailing of the tracer concentration curve with $V_{pro} > V_{inj}$.

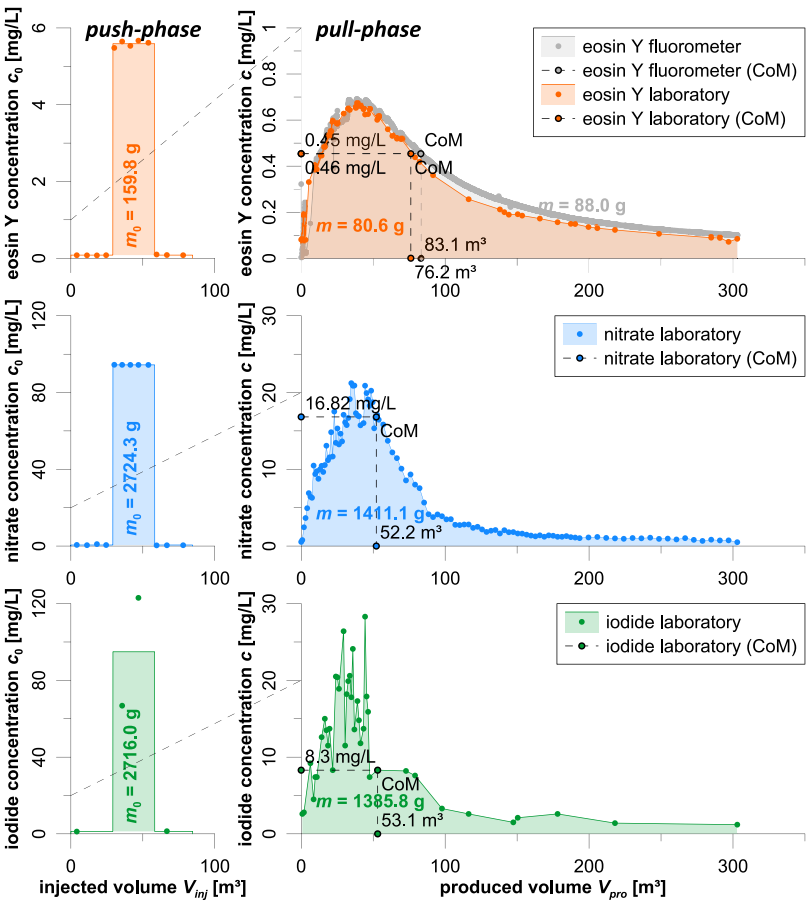

Fig. 9. Determined eosin Y, nitrate, and iodide concentrations during the 2nd Push–Pull Test (PPT2). For each tracer the Center of Mass (CoM) at which one-half of the mass of the tracer has been recovered is indicated.

derived. For PPT1 a Darcy velocity of $q = 1.27 - 1.37 \times 10^{-5}$ m/s and a hydraulic gradient of $I = 1.27 - 1.37$ m/m were calculated. In contrast, the results of PPT2 only show values of $q = 7.09 - 9.42 \times 10^{-7}$ m/s and $I = 0.07 - 0.09$ m/m.

From the tracer concentration curves of the pull-phases, the attenuation factor $\mathcal{X}$ and the longitudinal dispersivity a_L as well as the longitudinal dispersion coefficient D_L were derived. The attenuation factor was calculated based on Eq. (21) using the tracer concentration measured at the point where the volume produced was equal to the volume injected. The attenuation factor $\mathcal{X}$ for PPT1 (512 min shut-in period) was 2.6 (nitrate), 3.4 (iodide), and 3.8–3.9 (eosin Y). For PPT2 having a 19 335 min long shut-in period the attenuation factor was 2.9 (nitrate), 5.6 (iodide), and 4.4–4.6 (eosin Y). The tailing of the tracer curves ($V_{pro} > V_{inj}$) were used to determine the longitudinal dispersivity a_L by type curve analysis (Figs. 8 and 10). For PPT1 a longitudinal dispersivity of $a_L = 0.24 - 1.05$ m was obtained. The corresponding longitudinal dispersion coefficient was $D_L = 1.27 - 5.99 \times 10^{-5}$ m^2/sec. For PPT2 the longitudinal dispersivity and dispersion coefficient were $a_L = 0.33 - 1.39$ m and $D_L = 0.97 - 5.45 \times 10^{-6}$ m^2/sec.

3.4. Distributed Temperature Sensing (DTS)

Fig. 11 shows the DTS data over the timing of the fluid injection testing along the inner production casing and outer anchor casing. A schematic of the location of the fiber-optic cables is shown next to the temperature data. In the upper subplot, the fluid injection volumes and temperatures measured at wellhead and at the injection string at 212 m are shown.

During onset of hot water injection, the temperatures increase both in the production casing and the anchor casing. Temperatures in the production casing (closer to the injection string) are higher than on the outside. The highest temperatures are measured in the open-hole section at the location of the filtered casing interval (220 to 230 m) where the target reservoir horizon (Exter Formation) is located. The hot plume is visible up to 214 m, just below the transition of the anchor casing shoe. After stopping of hot water injection, temperatures reduce within one hour in the interval from 214 to 224 m from 67 °C to 48 °C. In the interval from 224 to 228 m, temperatures remain at higher values for a longer period. A temperature drop from 71 °C to 48 °C occurs during the following 35 h.

8 h after stopping of the hot water injection (32.4 h), a sudden cross-flow was observed in the open hole section (see Fig. 12). Within minutes, temperatures reduce in the interval from 224 to 228 m from 64.5 °C to 60.5 °C. Simultaneously, the depth interval from 214 to 223 m experiences a warming up from around 41 °C to 46 °C.

Further calculations regarding the heat flux and heat loss along the well based on the DTS data can be found in Appendix D.

4. Discussions

A comprehensive study to evaluate the use of the Exter Formation as an ATES was performed. This includes seven Slug-Withdrawal Tests (SWTs), one Step-Rate Test (SRT), and two Push–Pull Tests (PPTs) as

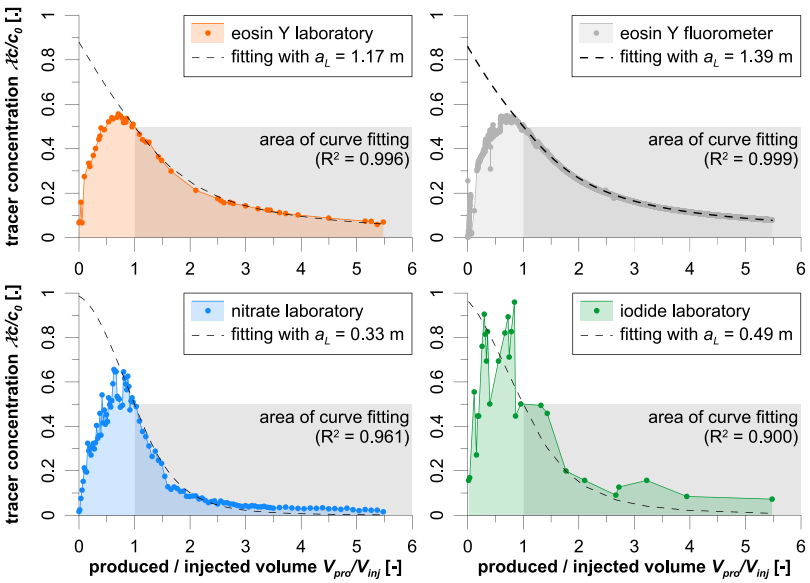

Fig. 10. Type curve analysis to determine the longitudinal dispersivity a_L for the 2nd Push–Pull Test (PPT2). The curve fitting was performed for the tailing of the tracer concentration curve with $V_{pro} > V_{inj}$.

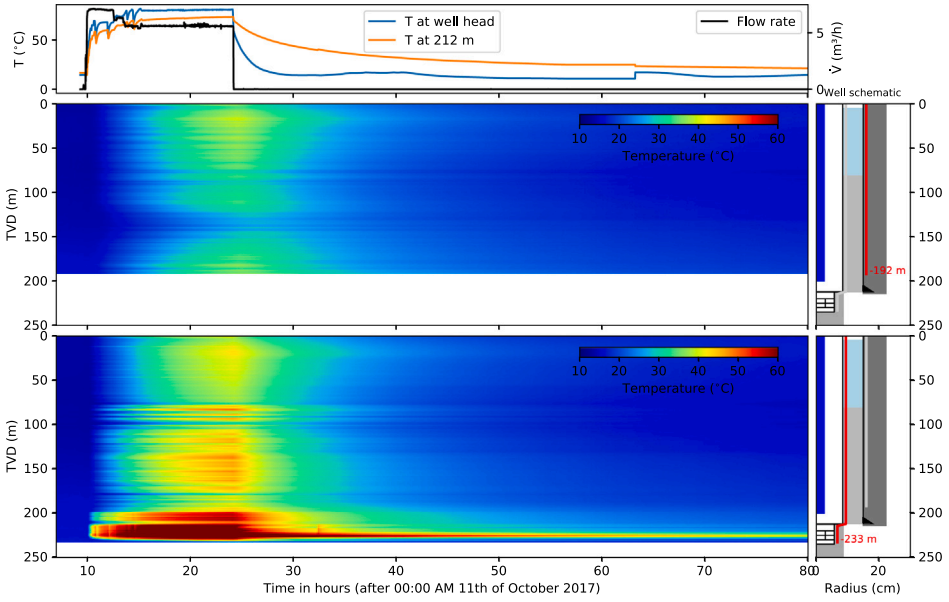

Fig. 11. DTS data during injection phase along the anchor casing (center subplot) and production casing (bottom subplot). The top subplot displays the injection flow rate and temperature at the wellhead and in the well at 212 m.

well as Distributed Temperature Sensing (DTS). The selection of the methodologies, their applicability and the possibility of improvement are discussed in Section 4.1. The resulting assessment of the use of the Exter Formation as an ATES is discussed in Section 4.2.

4.1. Limits of the methodology used

The SWTs were conducted to determine the potential alteration of the hydraulic aquifer performance caused by the SRT and by the two PPTs, especially by PPT2 with hot water. In comparison to the SRT, the SWTs provide a fast and cost-efficient alternative in determining the hydraulic characteristics of an aquifer. In our SWT an air compressor was used to generate additional wellhead pressure (15 min for 2 bar and 1 h for 5 bar). Theoretically, the additional wellhead pressure will lead to a drawdown of the water column in the borehole but will not significantly change the bottom-hole pressure. After achieving the additional wellhead pressure the compressed air was suddenly released by either by a 1 1/4″ (22.09.17) or a 2″ (02.11.17) pressure release valve. For the first series of SWTs (22.09.17) the pressure release valve was first opened and then the air compressor was switched off resulting in a non-stabilized bottom-hole pressure which made the analysis difficult. Therefore, we suggest waiting for the equalization of the bottom-hole pressure after turning of the air compressor as applied for the second series of SWTs (02.11.17). In our SWTs this pressure stabilization was achieved after approximately 300 s. To release 5 bar additional wellhead pressure via a 1 1/4″ (22.09.17) pressure release valve took 15–21 s. In contrast, only 7–8 s were required to release 5 bar via a 2″ pressure release valve 2″ (02.11.17). Since the release time strongly influences the ratio H/H_0 used for the analysis, we generally suggest to shorten the pressure release time to a technical minimum.

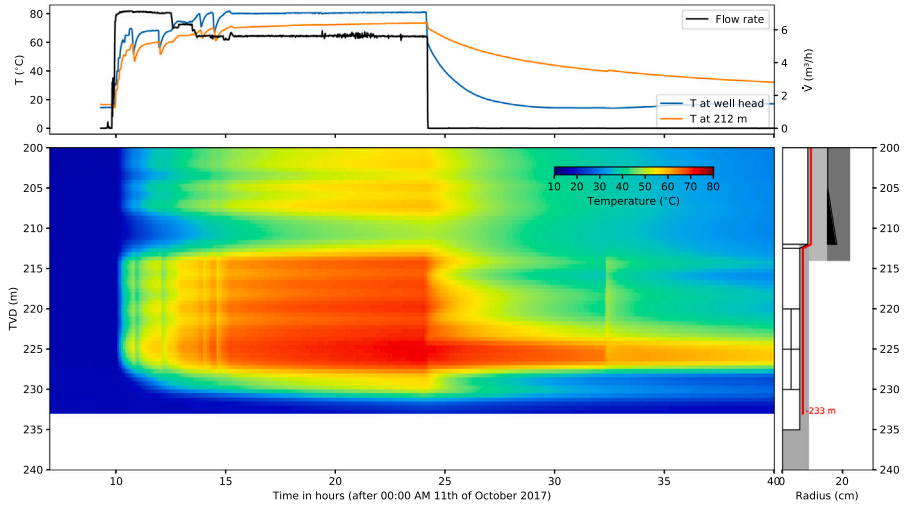

Fig. 12. DTS data during injection phase measured with the cable along the production casing (close-up from Fig. 11).

For the SRT, a series of five constant-rate steps with increasing production rates from 1.95 m^3/h to 6.30 m^3/h was performed. Each constant-rate step was performed on equal time length of approximately 2 h. This time was not sufficient to achieve steady state conditions in terms of bottom-hole pressure at the end of each step. We used the recorded pressure drawdown at the end of each step for the analysis. To determine a reliable PI for each step, we strongly recommend that steady state conditions must be achieved for the individual steps. Furthermore, the analysis of the individual steps and is corresponding drawdown indicates non-linear pressure losses at high flow rates. For the highest flow rate of 6.30 m^3/h the non-linear pressure losses led to an additional drawdown of 1.11 bar that is more than one-third of the total drawdown. Here, a better borehole and filter design could serve to achieve the potential productivity of $PI_{pot} = 1/B = 3.13\ m^3/(h\ bar)$.

During the two PPTs we pre-flushed the well before injecting the tracer and subsequently injected a chaser which is original groundwater without any added solutes. The objective of the chaser is to push the test solution out of the borehole into the aquifer and therefore to minimize the influence of the gravel pack on the shape of the breakthrough curve (Hebig et al., 2015). Since we used an injection string for the push-phase, the borehole volume was reduced to approximately $V_{bh} = 0.74\ m^3$. Therefore, the injected chaser volume of approximately 27 m^3 was too large and pushed the tracer out of the borehole and much further in the aquifer. During the pull-phase we could observe a clear influence of the tracer concentrations by the chaser because at the start of the pull-phase, the concentration ratio $\mathcal{X}c/c_0$ was not 1 as expected, but almost zero (Figs. 8 and 10). Therefore, only the tailing of the tracer curve could be analyzed. In accordance to Hebig et al. (2015) we suggest a chaser volume that is equivalent to the borehole volume plus the volume of the pore space of the gravel pack.

It is possible to use the same tracers for successive PPTs if their background concentrations are known. For both, artificial and naturally occurring tracer the background concentrations must be determined in advance to each PPT and the measured tracer concentrations must be corrected by these values. Here the analysis of previously pumped aquifer water or the analysis of the produced water at the end of the last pull-phase are best suited. For PPT2 we corrected the concentration values, since for this test the background concentration were increased by PPT1.

For quantifying the attenuation factor of the tracer we used the fact that theoretically the ratio c/c_0 must be 0.5 if the volume produced corresponds to the injected volume $V_{pro} = V_{inj}$. The concentration c/c_0 at $V_{pro} = V_{inj}$ was obtained by curve fitting. As shown in Figs. 8 and 10 only the data from the GGUN-FL30 flow-through field fluorometer have the quality to derive the attenuation factor. Furthermore, for analyzing the groundwater velocity and dispersivity, the data obtained in the laboratory could only be used to a limited extent because they show high fluctuations. For a better analysis, a higher data density must be achieved via a more frequent sampling, particularly during the push phase.

4.2. Evaluation of the encountered Exter Formation aquifer as an ATES

The results of the SRT indicate that the drilled aquifer, although only 4 m thick, is suitable for ATES. An aquifer transmissibility of $\mathcal{T} = 3.2 \times 10^{-5}\ m^2/s$ and the corresponding productivity index of $PI = 2.0\ m^3/(h\ bar)$ allow maximum flow rates of about 5 m^3/h. The performed SWTs indicate a higher transmissibility between $\mathcal{T} = 5.67 \times 10^{-5}\ m^2/s$ and $\mathcal{T} = 9.45 \times 10^{-5}\ m^2/s$. Since the SWTs do not reach the coverage radius of the SRT, the obtained results can therefore only be seen as a rough estimate of the transmissibility that is strongly influenced by the transmissibility of the gravel pack.

The low recovery factor (50%–65%) for the tracers and the fast temperature equilibration after the push-phase with hot water indicate no optimal conditions for an ATES. As mentioned in Section 2, the Rupelbasissand having an artesian discharge was improperly sealed by cementation. As shown in Appendix C, the Rupelbasissand is hydraulically connected to the Exter Formation via the gravel pack and the wellbore (Fig. 1). This was also confirmed by chemical analysis as described in Regenspurg et al. (2020). The overpressure in the Rupelbasissand leads to a flow from the Rupelbasissand to the Exter Formation during shut-in and standstill periods. Beside the distributed temperature sensing the obtained values for groundwater velocity, Darcy velocity, and hydraulic gradient indicate strong flow activities during shut-in periods. Comparing the results of PPT1 with PPT2 show, that the hydraulic gradient and all velocities are reduced by more than one order of magnitude. The applied methods consider the effect of injection and production on the tracer transport, however, cross-flow between different units is not considered. Therefore, the derived values for the velocities and hydraulic gradients provide a measure for the injection-triggered flow or cross-flow in the vicinity of the well.

Through numerical simulation, it is possible to assess or even completely ignore the influence of the injection triggered cross-flow on the long-term recovery efficiency. The geological information as well as the comprehensive hydraulic and thermal properties collected by the best practice approach proposed here make it possible to create such a model, parameterize it and calculate the energetic efficiency over several years.

5. Conclusions

At the ATES research well Gt BChb 1/2015 the Exter Formation was evaluated for its HT-ATES potential. The determined aquifer and well characteristics indicate its suitability for an ATES. The tested formation did not show any alteration of the hydraulic performance due to the injection of hot water. This fact was indicated by SWTs performed before and after the two PPTs. However, both PPTs and the temperature evolution indicate a strong cross-flow in the well. This strong cross-flow led to an attenuation of the injected fluid by a factor of 3–5, which would strongly decrease its ATES potential.

Generally, for a sustainable operation of an ATES the characteristics of the well and the aquifer during charging, discharging, and storage time have to be determined. The most important hydraulic properties of the well are the productivity index and the skin-effect and of the aquifer the transmissibility and storativity. During the storage time the stored heat should stay in place and no drift neither by natural groundwater flow nor by cross-flow should occur. Regarding the thermal properties, the heat capacity of the formation as well as the conductive heat loss from the well to the formation expressed by the thermal conductivity must be considered. Additionally, an alteration of these properties due to the ATES operation must be quantified. Therefore, we suggest as best practice, the following test procedure in chronological order:

- A well-development before starting the hydraulic tests should be performed. The end should be determined by achieving constant values for the chemical properties and the produced water be clear. At least 10 times of the borehole volume should be produced.
- For determining the productivity index and storativity a SRT with more than 3 steps should be performed. To determine a reliable productivity index, each step should achieve steady state conditions. More than 3 steps are required to determine the non-linear pressure losses having non-quadratic characteristics. From the build-up of the SRT the transmissibility and storativity can be derived.
  - If no submersible pump is installed the SRT can be performed as an air-lift test.
  - For economic reasons the transmissibility and storativity as well as productivity index can be estimated by SWTs. The coverage radius of the SWT is generally smaller than that of the SRT and therefore the results only represent the properties of the near vicinity of the borehole.
- A single well PPT with tracers should be performed to analyze not only the longitudinal dispersion and the natural groundwater velocity but also to derive the attenuation factor caused by cross-flow.
  - The longitudinal dispersion can be derived to characterize the gradient of the thermal front.
  - The natural groundwater velocity is the key parameter to estimate the drift of the injected hot water.
  - The attenuation factor can quantify the amount of cross-flow.
- The aforementioned PPT can be improved by injecting the tracers along with hot water and monitoring the temperature signal by DTS.
  - The DTS data can be used to identify the well inflow areas (profiling) along the filter screen.
  - Two DTS cables installed in different distances to the well can be used to determine the conductive heat flux from the well to the surrounding rocks.
  - The direction of potential cross-flow can qualitatively be estimated.
  - The general well integrity can be monitored.
- Either SRT or SWTs can be used to determine the alteration of the aquifer properties caused by hot water injection and storage by applying the same test procedure before and after a PPT with hot water.

The limits of the proposed test procedure are discussed and suggestions for adopting and improving it are provided. Furthermore, we suggest accompanying the analytical field test with a numerical simulation to validate the findings.

Declaration of competing interest

The authors declare that they have no known competing financial interests or personal relationships that could have appeared to influence the work reported in this paper.

Data availability

Data will be made available on request.

Acknowledgments

This work has been performed in the framework of the project “Effizienz und Betriebssicherheit von Energiesystemen mit saisonaler Energiespeicherung in Aquiferen für Stadtquartiere” [BMWi, FKZ03ESP409A], which were funded by the Federal Ministry for Economic Affairs and Energy (BMWi), Germany. We kindly acknowledge the Hydroisotop GmbH for iodide measurements.

Appendix A. Supplementary data

Supplementary material related to this article can be found online at https://doi.org/10.1016/j.geothermics.2023.102830.

References

Azizian, M.F., Istok, J.D., Semprini, L., 2005. Push-pull test evaluation of the in situ aerobic cometabolism of chlorinated ethenes by toluene-utilizing microorganisms. Water Sci. Technol. 52 (7), 35–40. http://dx.doi.org/10.2166/wst.2005.0178.

Bridger, D.W., Allen, D.M., 2005. Designing aquifer thermal energy storage systems. ASHRAE 6.

Chakraborty, M., Panda, A.K., 2011. Spectral behaviour of eosin Y in different solvents and aqueous surfactant media. Spectrochim. Acta A 81 (1), 458–465. http://dx.doi.org/10.1016/j.saa.2011.06.038.

Cooper, H.H., Bredehoeft, J.D., Papadopulos, I.S., 1967. Response of a finite-diameter well to an instantaneous charge of water. Water Resour. Res. 3 (1), 263–269. http://dx.doi.org/10.1029/wr003i001p00263.

Dinçer, İ., Rosen, M.A., 2010. Thermal Energy Storage: Systems and Applications. Wiley, http://dx.doi.org/10.1002/9780470970751.

Fleuchaus, P., Godschalk, B., Stober, I., Blum, P., 2018. Worldwide application of aquifer thermal energy storage – A review. Renew. Sustain. Energy Rev. 94, 861–876. http://dx.doi.org/10.1016/j.rser.2018.06.057.

Gao, L., Zhao, J., An, Q., Wang, J., Liu, X., 2017. A review on system performance studies of aquifer thermal energy storage. Energy Procedia 142, 3537–3545. http://dx.doi.org/10.1016/j.egypro.2017.12.242.

Gelhar, L.W., Collins, M.A., 1971. General analysis of longitudinal dispersion in nonuniform flow. Water Resour. Res. 7 (6), 1511–1521. http://dx.doi.org/10.1029/wr007i006p01511.

Gnielinski, V., 2013. G1 durchströmte Rohre. In: VDI-Wärmeatlas. Springer Berlin Heidelberg, pp. 785–792. http://dx.doi.org/10.1007/978-3-642-19981-3_42.

Hebig, K.H., Zeilfelder, S., Ito, N., Machida, I., Marui, A., Scheytt, T.J., 2015. Study of the effects of the chaser in push–pull tracer tests by using temporal moment analysis. Geothermics 54, 43–53. http://dx.doi.org/10.1016/j.geothermics.2014.11.004.

Horner, D.R., 1951. Pressure build-up in wells. In: Proc., Third World Pet. Cong., the Hague. pp. 503–523.

Hoth, K., Schretzenmayr, S., 1993. Die tiefen Bohrungen im Zentralabschnitt der Mitteleuropäischen Senke: Dokumentation für den Zeitabschnitt 1962 - 1990 ; mit zwei Tabellen. In: Schriftenreihe für Geowissenschaften, Verlag der Gesellschaft für Geowissenschaften, p. 145.

Istok, J.D., Humphrey, M.D., Schroth, M.H., Hyman, M.R., O'Reilly, K.T., 1997. Single-well, "push-pull" test for in situ determination of microbial activities. Ground Water 35 (4), 619–631. http://dx.doi.org/10.1111/j.1745-6584.1997.tb00127.x.

Jacob, C.E., 1947. Drawdown test to determine effective radius of artesian well. Trans. Am. Soc. Civ. Eng. 112 (1), 1047–1064.

Käss, W., 2004. Geohydrologische Markierungstechnik. Gebrüder Borntraeger.

Klepikova, M.V., Borgne, T.L., Bour, O., Dentz, M., Hochreutener, R., Lavenant, N., 2016. Heat as a tracer for understanding transport processes in fractured media: Theory and field assessment from multiscale thermal push-pull tracer tests. Water Resour. Res. 52 (7), 5442–5457. http://dx.doi.org/10.1002/2016WR018789.

Kruisdijk, E., van Breukelen, B.M., 2021. Reactive transport modelling of push-pull tests: A versatile approach to quantify aquifer reactivity. Appl. Geochem. 131, 104998. http://dx.doi.org/10.1016/j.apgeochem.2021.104998.

Langguth, H.-R., Voigt, R., 2013. Hydrogeologische Methoden. Springer Berlin Heidelberg.

Leap, D.I., Kaplan, P.G., 1988. A single-well tracing method for estimating regional advective velocity in a confined aquifer: Theory and preliminary laboratory verification. Water Resour. Res. 24 (7), 993–998. http://dx.doi.org/10.1029/wr024i007p00993.

Lee, P.K., Pearson, R., Leech, R.E.J., Dickin, R., 1982. Hydraulic testing of deep fractures in the Canadian shield. Bull. Int. Assoc. Eng. Geol. 26–27 (1), 461–465. http://dx.doi.org/10.1007/BF02594259.

Leibundgut, C., Maloszewski, P., Klls, C., 2009. Tracers in Hydrology. John Wiley & Sons, Ltd, http://dx.doi.org/10.1002/9780470747148.

Leibundgut, C., Seibert, J., 2011. Tracer hydrology. In: Treatise on Water Science. Elsevier, pp. 215–236. http://dx.doi.org/10.1016/b978-0-444-53199-5.00036-1.

Meigs, L.C., Beauheim, R.L., 2001. Tracer tests in a fractured dolomite: 1. Experimental design and observed tracer recoveries. Water Resour. Res. 37 (5), 1113–1128. http://dx.doi.org/10.1029/2000wr900335.

Milsch, H., Giese, R., Poser, M., Kranz, S., Feldbusch, E., Regenspurg, S., 2013. Technical paper: FluMo—a mobile fluid–chemical monitoring unit for geothermal plants. Environ. Earth Sci. 70 (8), 3459–3463. http://dx.doi.org/10.1007/s12665-013-2408-x.

Paradis, C.J., McKay, L.D., Perfect, E., Istok, J.D., Hazen, T.C., 2017. Push-pull tests for estimating effective porosity: expanded analytical solution and in situ application. Hydrogeol. J. 26 (2), 381–393. http://dx.doi.org/10.1007/s10040-017-1672-3.

Regenspurg, S., Alawi, M., Blöcher, G., Börger, M., Kranz, S., Norden, B., Saadat, A., Scheytt, T., Virchow, L., Vieth-Hillebrand, A., 2018. Impact of drilling mud on chemistry and microbiology of an Upper Triassic groundwater after drilling and testing an exploration well for aquifer thermal energy storage in Berlin (Germany). Environ. Earth Sci. 77 (13), http://dx.doi.org/10.1007/s12665-018-7696-8.

Regenspurg, S., Alawi, M., Norden, B., Vieth-Hillebrand, A., Blöcher, G., Kranz, S., Scheytt, T., Horn, F., Burckhardt, O., Rach, O., Saadat, A., 2020. Effect of cold and hot water injection on the chemical and microbial composition of an aquifer and implication for its use as an aquifer thermal energy storage. Geothermics 84, 101747. http://dx.doi.org/10.1016/j.geothermics.2019.101747.

Rockel, W., Brandt, W., Seibt, P., 1999. Ein mesozoischer Aquifer im Zentrum Berlins als saisonaler Wärmespeicher für Parlamentsbauten. Brandenbg. Geowiss. Beitr. 6 (1), 91–101.

Schnegg, P.-A., 2002. An inexpensive field fluorometer for hydrogeological tracer tests with three tracers and turbidity measurement. In: Articles of the Geomagnetism Group at the University of Neuchâtel. pp. 1484–1488.

Schroth, M.H., Kleikemper, J., Bolliger, C., Bernasconi, S.M., Zeyer, J., 2001. In situ assessment of microbial sulfate reduction in a petroleum-contaminated aquifer using push–pull tests and stable sulfur isotope analyses. J. Contam. Hydrol. 51 (3–4), 179–195. http://dx.doi.org/10.1016/s0169-7722(01)00128-0.

Wagner, V., Li, T., Bayer, P., Leven, C., Dietrich, P., Blum, P., 2013. Thermal tracer testing in a sedimentary aquifer: field experiment (Lauswiesen, Germany) and numerical simulation. Hydrogeol. J. 22 (1), 175–187. http://dx.doi.org/10.1007/s10040-013-1059-z.

Zenner, M.A., 2009. Near-well nonlinear flow identified by various displacement well response testing. Ground Water 47 (4), 526–535. http://dx.doi.org/10.1111/j.1745-6584.2009.00545.x.